



Influence of Au/Pd alloy on amine functionised ZnCr LDH-MCM-41 nanocomposite; a visible light sensitive photocatalyst for one-pot Imines synthesis

Journal:	<i>Catalysis Science & Technology</i>
Manuscript ID	CY-ART-12-2018-002603
Article Type:	Paper
Date Submitted by the Author:	26-Dec-2018
Complete List of Authors:	Sahoo, Diptiprava; Institute of Technical Education and Research,, Chemistry Patnaik, Sulagna; ITER, SOA University, Centre for Nano Science and Nano Technology Rath, Dharitri; Rajdhani College, Bhubaneswar-751003 mohapatra, Priyabrat; C.V.Raman College of Engineering, Bidyanagar, Mahura, Janla, Bhubaneswar- 752 054 Mohanty, Ashutosh; Indian Institute of Science - [IISc], Bangalore Parida, Kulamani; SOA University, Centre for Nano Science and nano technology

Article type: Full paper

**Catalysis
Science &
Technology**



Website www.rsc.org/catalysis

Impact factor* 5.365

Journal expectations To be suitable for publication in *Catalysis Science & Technology* articles must show new catalytic discoveries that are a significant advance on previously published work.

Article type: Full paper Original scientific work that has not been published previously. Full papers do not have a page limit and should be appropriate in length for the scientific content.

Journal scope Visit the [Catalysis Science & Technology website](http://www.rsc.org/catalysis) for additional details of the journal scope and expectations.

Original research articles published in the journal must show new catalytic discoveries that are a significant advance on previously published work, bringing conceptual advances, or molecular insights to catalytic processes, and where appropriate, demonstrate the relationship between synthesis, structure and performance of catalytic systems. Kinetics and mechanisms are a central part of catalysis science and should be included in submitted articles. Examples of topics within the journal's scope are:

- In-depth mechanistic insights through advanced methods and theoretical methods that are of significant and direct interest and impact in the science and application of catalysts and catalytic processes. Studies using concepts are preferred to trial and error optimisation
- New catalysts and/or processes for conversions of current and future interest within life sciences, pharmaceuticals, polymers, environmental protection, energy and fuels. Studies that report incremental improvement of catalytic performance will not be published in the journal
- New catalytic reactions with significant impact in addressing current challenges and societal demands, for example waste reduction, reduced energy use or efficient use of feedstocks
- Studies that relate chemical reactions at surfaces, reactivity of metal complexes, or macromolecular structure to catalytic function and processes. Studies emphasising sophisticated materials and properties with residual evidence of catalytic function will not be published in the journal
- Theoretical studies of materials and molecules (exhibiting catalytic turnover) that result in significantly greater performance or understanding of existing catalytic reactions
- Studies on multiscale modelling, for example, engineering of catalytic processes from the nano to the macroscale
- Synthesis strategies for inorganic materials, hybrid materials and macromolecules that can be used as catalysts or their supports. Studies that claim catalyst performance must support this with kinetic data and proper mass balances

Reviewer responsibilities Visit the [Reviewer responsibilities website](http://www.rsc.org/catalysis) for additional details of the reviewing policy and procedure for Royal Society of Chemistry journals.

When preparing your report, please:

- Focus on the originality, importance, impact and reliability of the science. English language and grammatical errors do not need to be discussed in detail, except where it impedes scientific understanding.
- Use the [journal scope and expectations](http://www.rsc.org/catalysis) to assess the manuscript's suitability for publication in *Catalysis Science & Technology*.
- State clearly whether you think the article should be accepted or rejected and include details of how the science presented in the article corresponds to publication criteria.
- Inform the Editor if there is a conflict of interest, a significant part of the work you cannot review with confidence or if parts of the work have previously been published.

Thank you for evaluating this manuscript, your advice as a reviewer for *Catalysis Science & Technology* is greatly appreciated.

Dr Katie Lim Executive Editor
Royal Society of Chemistry, UK

Professor Piet van Leeuwen Editor-in-Chief
Université de Toulouse, France



Cover letter

Date: 27/12/2018

Prof. K. M. Parida, PhD, D.Sc, FRSC, CChem

Director, Centre for Nano Science and Nano Technology

ITER, Siksha O Anusandhan Deemed to be University

Bhubaneswar-751030

To

The Editor

Catalysis Science & Technology

Dear Sir,

Thank you very much for giving us the opportunity to revised our manuscript entitled **“Influence of Au/Pd alloy on amine functionlised ZnCr LDHMCM-41 nanocomposite; a visible light sensitive photocatalyst for one-pot Imines synthesis.”** by Dipti Prava Sahoo, Sulagna Patnaik, Dharitri Rath, Priyabarta Mohapatra, Asutosh Mohanty and Kulamani Parida *“Nanoscale”* as a full paper. We have also honestly thanks the referees for their constructive evaluations on this manuscript CY-ART-08-2018-001788 and they have raised numerous positive suggestions, which are extremely important to further improve the quality of our work. As for the detailed concerns of the referees, we have explained him by point-to-point in a separate file of response to referee’s comment and highlighted the changes made by us in the revised manuscript with red colour.

Hope the present form of manuscript is suitable for publication in your esteemed journal "*Nanoscale*".

Thanking you,

With best regards,

(Dr. K.M. Parida)

Response to reviewers comments

We are extremely obliged and grateful to the reviewers for reviewing the manuscript and for their scientific suggestions to improve the quality of the manuscript.

Referee: 1

Comments to the Author

1. Systematic decrease in the pore volume reported in Table 1 indicates an increasing pore blockage from MCM-41 to ALM-AuPd. I feel the amount of LDH anchored on MCM-41 might be too large and by decreasing the amount of LDH (and increasing its dispersion), higher activity could be achieved. Author may want try this.

Ans. Taking into consideration the increased pore blockage from MCM-41 to ALM-AuPd as per the reviewer's valuable suggestion, we have prepared three more nanocomposite excluding ALM (weight ratio between LDH to MCM-41 is 1:1) with varying the weight ratio between LDH to MCM-41 like 0.5:1 (AL_{0.5}M), 0.33:1 (AL_{0.33}M) and 0.2:1 (AL_{0.2}M) and evaluated the photocatalytic activity towards benzyl alcohol conversion. Among all, ALM (weight ratio between LDH to MCM-41 is 1:1) showed better conversion efficiency with higher yield and selectivity (Table s1). Although pore blockage was increased with increasing the LDH concentration, it makes available of a large number of active sites for photocatalytic reaction. MCM-41 is not a visible light responsive material it gives only high surface area as a support. In this study our purpose of using maximum amount of LDH is to provide sufficient exposed surface –OH groups for grafting of amine groups and to promote uniform dispersion of noble metal nanoparticles (Au, Pd and Au/Pd alloy) onto the surfaces of the catalyst without aggregation.

2. If the reported Au 4f BE is correct, it should be interpreted as anionic gold. Metallic gold 4f_{7/2} core level appears at 84 eV, and reduction in BE by 0.5 eV to 83.5 eV justifies that it has acquired electrons; or at least there is some charge transfer from ligand. Indeed anionic gold occurs due to proper metal-semiconductor junction and charge transfer from semiconductor/ligand occurs to gold. Pl. see Nanoscale 2015, 7, 11206 and cite.

Ans. Thank you for your keen observation. We further calibrated (C 1s reference peak at binding energy of 284.9 eV) and deconvoluted the ALM-Au/Pd nanocomposite. The result shows the binding energy of Au 4f_{7/2} and Au 4f_{5/2} was observed at 83.7 eV and

87.4 eV respectively which is quite negative compared to your suggested article (Nanoscale 2015, 7, 11206, Ref no.-54, 22) and our reported reference article (*Catal. Sci. Technol.*, 2018, 8, 268-275). We have also cited your suggested article in manuscript. The negative shifting in binding energy of Au 4f suggests the drift of electrons from the smaller electronegativity of Pd (2.2) to larger electronegativity of Au (2.4), and supports the formation of Au/Pd alloy structure (*ACS Sustainable Chem. Eng.*, 2017, 5, 5852 – 5861. Ref no.-24).

3. Photo included for material colour may be simply identified with letter a, b, c... as given in figure legend (Fig. 5). Arrows are confusing. Photo may be placed inside the panel horizontally, to minimize the space. Letter (a) is given twice in Fig. 5 and it should be removed from the top.

Ans. According to the reviewer's valuable suggestion, we have removed the arrows from Fig. 5, inserted the material colour inside the panel horizontally and corrected the notations. Letter (a) was also removed from the top of the figure (Fig. 5).

4. Au with Pt, Pd or Ag bimetal supported on titania was reported for water splitting (Nanoscale 2015, 7, 13477) and it may be briefly mentioned in the introduction. How authors determine that the Au-Pd is present as alloy, but not in other form (bimetal, core-shell etc.).

Ans. As per the suggestion of the esteemed reviewer, we have included the above related references in the revised manuscript. (Ref no.- 10).

We have again carried out the XRD analysis of ALM-Au/Pd nanocomposite. From XRD results (Figure 1b) it was found that two peak at 38° and at 40° are obtained representing (111) basal planes of Au and Pd nanoparticles in ALM-Au and ALM-Pd monometal nanocomposite respectively. However, upon loading bimetallic Au/Pd nanoparticles, a weak broad diffraction peak was observed between 2θ of 38° to 40° (inserted the deconvoluted image of weak broad diffraction peak of ALM-Au/Pd). The peak position in case of bimetallic alloyed nanoparticles clearly indicated an intermediate scattering angle. In addition, slight shifted in the diffraction peaks of the bimetallic nanoparticles was observed from ALM-Au to ALM-Pd. This confirmed the formation of Au-Pd alloys nanoparticles in ALM-Au/Pd nanocomposite rather than the simple mixture of bi metal nanoparticles. From XPS technique (Fig 4g and 4h) we have also proved the formation of Au/Pd alloy. After the formation of alloy between Au and Pd in ALM-Au/Pd nanocomposite, the binding energy of Au 4f was

shifted towards negative value ($4f_{7/2}$ - 83.7 eV and $4f_{5/2}$ - 87.4 eV) whereas the spectrum of Pd 3d situated at higher binding energy ($3d_{5/2}$ -335.7 eV and $3d_{3/2}$ -341.5 eV) with relative to monometallic reported value. (Ref no.-22). This peak sifting indicates a close electronic interaction between Au and Pd in the created alloyed nanoparticle. In other words, the electron mobility takes place from the smaller electronegativity of Pd (2.2) to larger electronegativity of Au (2.4). This is also satisfied for formation of Au/Pd alloy structure. Moreover in UV-Vis DRS (Fig. 5b), after loading of Au nanoparticles, ALM-Au should show LSPR peak around 520 nm, however in this case a broad absorption peak was appeared as the LSPR peak overlaps with the MMCT band of ALM. Moreover, upon loading Pd nanoparticles the LSPR band of Au nanoparticles disappeared and a broad with less intensified peak was observed at about 520-570 nm (ALM-Au/Pd). The combination of Au atoms with Pd atoms, results to change in the colour of the sample from purple to gray. Further, the HRTEM image of ALM-Au/Pd (Fig. 2e) show the lattice fringes with an intermediate interplanar basal spacing of about 0.230 nm, which is slightly lower than the lattice spacing of metallic Au (d_{111} =0.235 nm) but higher than the metallic Pd lattice spacing (d_{111} =0.225 nm). This change in interplanar lattice spacing value clearly confirms the formation of bimetallic alloyed Au/Pd nanoparticles. It has been reported that incorporation of Pd into the crystal lattice of Au changes the crystal structure of Au and form alloy structure in between them. (Ref no.- 25). Conclusively it can be said that XRD, XPS UV-Vis DRS and HRTEM techniques support the formation of Au/Pd alloy in ALM-Au/Pd nanocomposite.

5. Direct solar oxidation of alcohol to aldehyde is reported in J. Mater. Chem. 2011, 21, 2639 should be referred in the introduction. Similarity benzene to phenol is also reported in ACS Catal. 2014, 4, 2844 and may be discussed in introduction.

Ans. As per the reviewer's suggestion, we have cited these above related articles in the revised manuscript. (Ref no.-11 and 42).

Referee: 2

Comments to the Author

1. Extra amount of benzyl alcohol (500% more than nitrobenzene) was applied in this work. It means this process generated great amount of "byproduct" (benzaldehyde),

nearly five times more than the "main product" (imine), which may make this reaction process meaningless.

Ans. To further clarify the comment, we have again performed the photocatalytic activity towards one-pot imine synthesis via photooxidation of benzyl alcohol and the photoreduction of nitrobenzene by reducing the concentrations of reactants. Here the proportion of benzyl alcohol (3mmole) to nitro benzene (1mmole) is 3:1 according to reported literature (Ref no.-35). Because photocatalytic reduction of 1 mol nitrobenzene require 6 mol proton (H^+) which produce from 3 mol of benzyl alcohol. This process obviously generated great amount of benzaldehyde but benzaldehyde is not a byproduct, it is also a desired product required for the formation of imine. Additionally 1 mol imine is produced by condensation reaction of 1 mol benzaldehyde with 1 mol aniline. So after the completion of tandem reaction the concentration of benzaldehyde should be two times of imine.

2. The band gap of LDH and ALM indicates ability of harvesting visible light. And it seems that the support ALM contributes to the major light absorption (Fig.5) and photo-promoted current transportation (Fig.8) for the Au-ALM, Pd-ALM and Au/Pd-ALM catalysts probably due to low loading of noble metal. So in this concern, the photo-generated hole and electron should play the dominating role in the photocatalytic reaction instead of the hot hole and electron derived from LSPR on the metal nanoparticles. Moreover, the authors deduced the reaction mechanism mainly according to ref.12 and ref.13. However, the catalysts in ref.12 and ref.13 employed ZrO_2 and ZnO as supports which cannot be excited under visible light. So the authors ignored the role of photo-generated hole and electron of the support and may result in a misleading mechanism.

Ans. Thank you for your's valuable suggestion. As per your suggestion, we re-evaluated the photocatalytic performance of all the as-synthesized materials towards imine formation through benzyl alcohol oxidation and nitrobenzene reduction. Thereafter the scavenger experiment was carried out for ALM-Au/Pd nanocomposite. Further we have calibrated and deconvoluted the XPS spectra of ALM-Au/Pd. Based on modified XPS results and the outcome from the scavenger experiment; the proposed mechanism was corrected by including the role of photogenerated electron and holes of LDH.

3. The discussion about the alloy formation in XRD patterns (Fig.1b) is not convincing. The detailed deconvolution pattern of ALM-Au/Pd. It seems that the

weak broad diffraction peak locates at 38° instead of between 38° to 40° as the authors claimed. Whatever, such discussion based on XRD patterns is not convincing because of the poor resolution. CO-absorbed FT-IR may be helpful to verify the formation of AuPd alloy on ALM.

Ans. We thank the reviewer for this valuable suggestion that is quite useful for improving the quality of this work. We have again prepared the ALM-Au/Pd nanocomposite and investigated the XRD analysis. Now the weak broad diffraction peaks of ALM-Au/Pd locates in between the Au [(111), 38°] and Pd [(111), 40°]. We have also deconvoluted the broad and less intense peak of ALM-Au/Pd and inserted in XRD image (Fig. 1b). Now the peak position in case of bimetallic alloyed nanoparticles clearly indicated an intermediate scattering angle. In addition, slight shifted in the diffraction peaks of the bimetallic nanoparticles was observed from ALM-Au to ALM-Pd. This confirms the formation of Au-Pd alloys nanoparticles in ALM-Au/Pd nanocomposite rather than the simple mixture of bi-metal nanoparticles. In addition, Han et al. also reported the diffraction peaks of the bimetallic particles exhibit a shift from pure Au to pure Pd as the Pd content increases which suggest that the prepared nanoparticles were Au-Pd alloys form. (Ref no.-40). Actually the Pd nanoparticles entered into the crystal lattice of Au nanoparticles resulting in the formation of alloyed nanoparticles due to slight mismatch in their lattice structure. Au lattice have tendency to capture the Pd lattice, revealed to close interaction between them and helped to produce of Au/Pd alloy nanoparticle. Moreover XPS UV-Vis DRS analysis also support the formation of Au/Pd alloy in ALM-Au/Pd nanocomposite. It may be help full by analysing the CO-absorbed FT-IR to verify the formation of AuPd alloy on ALM, but we have lack of experimental facilities for doing that characterisation.

4. The XPS results and relative discussion are doubtful. The C 1s spectra of carbon are commonly set as 284.6 eV for charge calibration, which is also clearly demonstrated in Materials Characterization section. However, in Fig.4, the C 1s binding energy of LDH and ALM-Au/Pd catalysts was shown as 284.9 eV and 284.1 eV, respectively. So we suspect that in this manuscript, the binding energy was not correctly calibrated, hence the relative discussion was doubtful.

Ans. Thank you for this comment. .Obviously the C 1s spectra of carbon are commonly set as 284.6 eV for charge calibration. But we consulted the XPS technician who uses VG Microtech Multilab ESCA 3000 spectrometer with Mg $K\alpha$

X-ray equipped with nonmonochromatized source. So as per the used XPS spectrometer, the 1s spectra of carbon at binding energy of 284.9 eV was taken for charge calibration.(Ref no.-59) In this aspect, the XPS survey of pure LDH is correct but we have again calibrated and deconvoluted the XPS spectra of ALM-Au/Pd and modified the discussion part with respect to XPS plot.

5. According to the pore size distribution plot Fig.1(d), there should be minor pore in ALM. But this is not consistent with the results in Table 1 that the pore volume and average pore size of ALM are comparable to those of LM and ALM-Au/Pd.

Ans. Thank you for your depth observation, we have modified the pore size distribution plot (Fig.1d) according to results in Table 1.

6. There are many obvious and careless mistakes in the manuscript. For instance, the imine yield displayed in Fig.6 (b) does not match the t data in Table S1 and relative discussion. And in Fig.6 (c) and (d), the labels were obviously wrong.

Ans. As per the discrepancy pointed out by the reviewer, we have thoroughly checked and corrected the mistakes in the manuscript. And according to your suggestion, we have again evaluated the photocatalytic performance of all as-prepared materials towards one-pot imine synthesis via photooxidation of benzyl alcohol and reduction of nitrobenzene. Furthermore we have changed the data and given in Table S2 and Fig.6 (a), (b) (c) and (d) with respect to the results of photocatalytic activity. The discussion part of photocatalytic activity in manuscript was also changed. And as per your suggestion, we correctly labelled the Fig.6 (c) and (d).

Influence of Au/Pd alloy on amine functionalised ZnCr LDH-MCM-41 nanocomposite; a visible light sensitive photocatalyst for one-pot Imines synthesis

Dipti Prava Sahoo^a, Sulagna Patnaik^a, Dharitri Rath^b, Priyabarta Mohapatra^c, Asutosh Mohanty^d and Kulamani Parida^{a*}

^aCentre for Nano science and Technology, Siksha ‘O’ Anusandhan Deemed to be University, Bhubaneswar-751030, Odisha, India

^bDepartment of Chemistry, Rajdhani College, Bhubaneswar-751003, Odisha, India

^cDepartment of Chemistry, C.V.Raman College of Engineering, Bidyanagar, Mahura, Janla, Bhubaneswar- 752 054, Odisha, India

^dSolid State and Structural Chemistry Unit, Indian institute of Science, Bengaluru-560012, India

Abstract

Achieving green photocatalytic organic transformation reaction by using visible light induced semiconductor based photocatalyst has been promising as a green and sustainable approach. In the present study, Au/Pd bimetallic alloy loaded amine (APTES) functionalised LDH-MCM-41 composite was prepared through in-situ co-precipitation followed by co-reduction method. The structural phase, textural property, optical behaviour, morphological aspects, chemical state and functional group of the photocatalysts were thoroughly analysed by PXRD, HRTEM, UV-Vis DRS, FTIR and XPS techniques. Moreover the formation of alloying structure between Au and Pd is confirmed from XRD, HRTEM and UV-Vis absorption spectra. One-pot synthesis of imines through photoalkylation benzyl alcohol with nitrobenzene over Au/Pd bimetal alloyed loaded on amine functionalised LDH-MCM-41 composite was investigated and it demonstrated imines yield of around 3.1 times (68%) than parent LDH (22%). The alloy nanoparticles efficiently harvest light and possess higher photocatalytic activity with respect to single Pd and Au nanoparticle. Alloying structure develops charge heterogeneity on the surface of alloyed nanoparticles and enhances the interaction between metal surface and substrate molecule which promotes the coupling between photo generated benzaldehyde with aniline to form imine. The characterisations such as PL, TRPL, EIS and photocurrent density further prove that the superior photoactivity towards imine synthesis. These photocatalytic tandem reactions, therefore, have a great

potential as an effective pathway for one-pot organic synthesis and transformation of organics in an environmentally friendly way.

*Corresponding Author: kulamaniparida@soauniversity.ac.in (K.M. Parida)

Introduction

Imines are superior group of organic compounds having carbon-nitrogen bond, which are very essential intermediates of various biological, pesticides, polymer and medicines product because they can undergo versatile organic conversion such as condensations, additions, reductions, and multi component reactions.¹ To serve the purpose, fabrication of basic unit imine is essential. The approach to imine synthesis has been adopted through photochemical reactions and various traditional methods. Although the designing of complicated organic transformation for imine formation, photochemical reactions are admirable, but are associated with low selectivity of targeted product make the process difficult.² Traditionally, with the support of lewis acid catalyst, the aldehydes/ketones undergoes dehydrating condensation reaction with amines to form imine. Further with more a simpler approach, dehydrogenation of secondary amine to form imine is also possible by using some strong oxidising agents like MnO₂ and *o*-iodoxybenzoic acid. However, adaptation of such synthesis route provides a low stability expensive pathway, difficulty in controlling the reaction condition, low selectivity of target products with plenty of undesired by-products generated from those oxidising agents. Various research groups also reported, the quick condensation of aldehydes and amines in presence of Lewis acid as catalysts at room temperature but this rapid oxidation process doesn't led to a dreamt successful reaction.³⁻⁶ To circumvent these difficulties, research has been accredited from photochemical and traditional method to photocatalytic reactions that can be executed under easily available conditions to achieve higher product selectivity.⁷ Further, integration of photocatalytic reaction into tandem reaction facilitates multi step reactions in one reactor and considered as an active approach to enhance chemical reactions. The approach bypasses time consumption, unwanted intermediates formation, lengthy separation purification process, energy utilization and loss of production.⁸ Many organic transformation reactions has been reported which are carried out in one pot tandem reaction. But many of these engage homogeneous catalysts, which result contaminated product and restricts recyclability.⁹ So, current research is focused on the development of a heterogeneous photocatalytic system, involving one-pot synthesis. In this one-pot synthesis route of imine,

the alkylation of benzyl alcohol (alkylating reagent) with nitrobenzene in the cooperation of heterogeneous photocatalyst is one of the most promising approaches due to easy accessibility, reasonable price, low energy consumption, environmental friendliness, reusability, and durability.⁷ In this context of one-pot imine synthesis, many visible light induced photocatalyst were studied for organic conversions that usually involves the following three consecutive steps: (i) photooxidation of benzyl alcohol to benzaldehyde, (ii) photoreduction of nitrobenzene to aniline, (iii) and finally condensation of benzaldehyde with aniline to form imine.

Moreover, the noble metals (Au, Pd, Ag, Pt and Cu) supported catalyst were efficiently used in various photocatalytic reactions like water splitting organic conversion, organic pollutant degradation, etc.^{10, 11} Among them bimetallic alloy catalyst (Au/Pd) in photocatalytic organic transformation reactions are important as they provide a greater activity result compared to single metal, as Au/Pd bimetallic alloy nanoparticles have a synergistic electron interaction between them that can enhance the photocatalytic performance. Further, upon visible light irradiation by the effect of LSPR, the energetic electrons (hot electrons) get transferred from Au to Pd due to electronegativity difference between the two atoms. As a consequence, electron availability in the Pd site proffers a good affinity for activating the reactant molecules. The charge heterogeneity on the surface of Au/Pd alloy nanoparticles plays vital role in photocatalytic reaction.¹² Various literatures are reported on Au/Pd alloy supported semiconductor materials like TiO_2 ,¹³ BiPO_4 ,¹⁴ $\text{g-C}_3\text{N}_4$,¹⁵ $\text{MOF}(\text{UiO-66}(\text{Zr}_{100-x}\text{Ti}_x))$,¹⁶ etc towards photocatalytic reaction. Additionally, the nature of support material is also very much important in organic conversion reaction. The surface acidity and basic sites stimulate the adsorption of substrate molecule to generate intermediate complexes which facilitates the reaction.

LDH play an important role in heterogeneous catalysis such as: (1) cation-tunability of the brucite-like layers and anionic exchangeability, (ii) tunable basicity of the surface both as Bronsted and Lewis type basic sites.¹⁷ By considering the surface basic properties of LDH, it has have progressively received much attention in various organic transformation reactions like condensations (Knoevenagel and aldol), trans-esterification and isomerisation.¹⁸⁻²⁰ (iii) uniform distribution of bivalent and trivalent metal cations in the brucite layer as well as preferred orientation of intercalated anions, offering the formation of highly dispersed and stable metal supported catalysts.¹⁷ Moreover LDH is a very good visible light based semiconductor photocatalyst having various important characters such as efficient light

harvesting power, tunable band gap energy, effective electron-hole separation and improved surface reaction kinetics.²¹ Till date, many scientists have studied Au/Pd alloy decorated LDH nanocomposite for photocatalytic and catalytic application. Wang et al. reported Au-Pd/MgAl LDH for enhancing photocatalytic towards selective oxidation of benzyl alcohol.²² Sobhana et al. studied Au/Pd nanoparticles decorated LDH for photodegradation of Orange II from water.²³ In another study, Gao et al. investigated the aerobic oxidation of 5-hydroxymethylfurfural in water over a highly energetic Au/Pd loaded Lanthanum doped Ca-Mg-Al LDH catalyst in a base free medium.²⁴

The direct loading of noble metal on LDH surface leads to formation of agglomerated metal nanoparticles. Therefore to improve the loading of Au/Pd NPs, the surface of LDH is functionalized by amine group. Previously our group has studied the primary alcohol oxidation and Suzuki coupling reaction by taking Pd(II) immobilised diamine functionalized LDH and Pd nanoparticles anchored on amine functionalized ZnAl-LDH catalyst, respectively.^{25,26} Although, LDH possess good potential support for functionalising with amine groups, but usually its surface area is very low and cannot provide sufficient exposed surface -OH groups for grafting of amine groups. Therefore modification of LDH with MCM-41 gives a large surface with silanol groups and mesoporous channels which can enhance the anchoring sites for amine groups attachment and also promotes the mass transport of reagents to and from the surface. Metal ions substituted in the MCM-41 framework behave as redox active sites which can be utilised for various catalytic condensation reactions.²⁷ The support material after functionalization promotes uniform dispersion of metal ions onto the surfaces of the catalyst without aggregation. The surface functionality, not only served as interaction sites for stabilising the metallic nanoclusters but also play a crucial role in photocatalytic organic conversion.²⁵

Based on the above considerations, in this study we have tried to synthesise Au/Pd alloy nanoparticles anchored on the amine (APTES) functionalized LDH/MCM-41 nanocomposite, for photocatalytic one-pot imine synthesis through photoalkylation of benzyl alcohol with nitrobenzene. The main advantages of using MCM-41 in the present study are large mesopores which provides mass transfer and the very large surface area allows a more active sites for reactions. The Bronsted and Lewis basic sites in amine functionalized LDH/MCM-41 helps to facilitate the deprotonation of surface adsorbed benzyl alcohol and precede the photocatalytic transformation reaction. The use of functionalised APTES group as a robust π -acidic monodentate nitrogen ligand, get attached covalently with -OH groups of LDH and MCM-41 to stabilize the Au/Pd alloy catalyst used in photocatalytic organic

conversion. The heterogeneity charge distribution of Au/Pd alloyed surface may improve the interaction between reactant molecule which reveal lowering in activation energy of the reaction and increasing photocatalytic conversion.

Experimental section

Materials.

Zn (NO₃)₂.6H₂O (98%), Cr(NO₃)₃.6H₂O (99%), NaOH (97%), Na₂CO₃ (99.5%), Cetyl Trimethyl Ammonium Bromide (CTAB), tetraethylorthosilicate (TEOS), NH₄OH, HAuCl₄, PdCl₂, KCl, NaBH₄, Benzyl alcohol, Benzaldehyde, Nitrobenzene, Aniline, N-benzylideneaniline (Imine) and Acetonitrile were purchased from Sigma Aldrich, Acros Organics, Merck and HIMEDIA. All the reagents in this research experiment are analytically pure grade. During the experiments, double distilled water was used.

Synthesis of MCM-41

Briefly, CTAB (2.4 g) was taken in 120 mL of water at room temperature. After obtaining a clear solution, 8 mL of NH₃ solution was added into it. Then silica source (TEOS, 10 mL) was allowed to mix with the above solution under continuous stirring. Immediately after hydrolysis, TEOS results a milky slurry of white precipitate. The resultant precipitate was stirred for another 3 h. Then it was allowed to dry at 80⁰C for overnight. To remove the surfactant, the collected white powder was calcined at 550⁰C for 5 h with a ramping rate of 5⁰C min⁻¹.²⁸

Synthesis of ZnCr LDH-MCM-41 (LM)

ZnCr LDH-MCM-41nanocomposite was fabricated by in-situ coprecipitation process. In concise, a desired amount of MCM-41 was taken in 20 mL water and dispersed for 30 min by ultrasonicator. A 200 mL of solution containing Zn(NO₃)₂.6H₂O and Cr (NO₃)₃.6H₂O with 2:1 molar ratio was slowly added to the above dispersed solution. Alkali solution containing 1 M Na₂CO₃ and 1 M NaOH was added drop wise manner to the above suspension maintaining pH of the solution at 8-9. In order to remove the extra dissolve ions, the obtained precipitate was filtered and washed for several times using distilled water. Then the product was dried at 80⁰C in air oven. ZnCr LDH-MCM-41nanocomposite was prepared with varying the weight ratio between LDH to MCM-41 like 0.2:1 (L_{0.2}M), 0.33:1 (L_{0.33}M) 0.5:1 (L_{0.5}M) and 1:1 (LM). For comparison study pure LDH was also prepared.

Synthesis of amine@ ZnCr LDH -MCM-41 (ALM)

1 gm of ZnCr LDH-MCM-41nanocomposite (L_{0.2}M, L_{0.33}M, L_{0.5}M and LM) was taken in 30 mL toluene in a round bottom flask, 0.6 mL of APTES (amine source) was poured drop wise

manner into this suspension and refluxed for 8 h. Then the resulted suspension was collected by centrifugation with ethanol-water solution and dried at 35°C for 12 h.²⁹

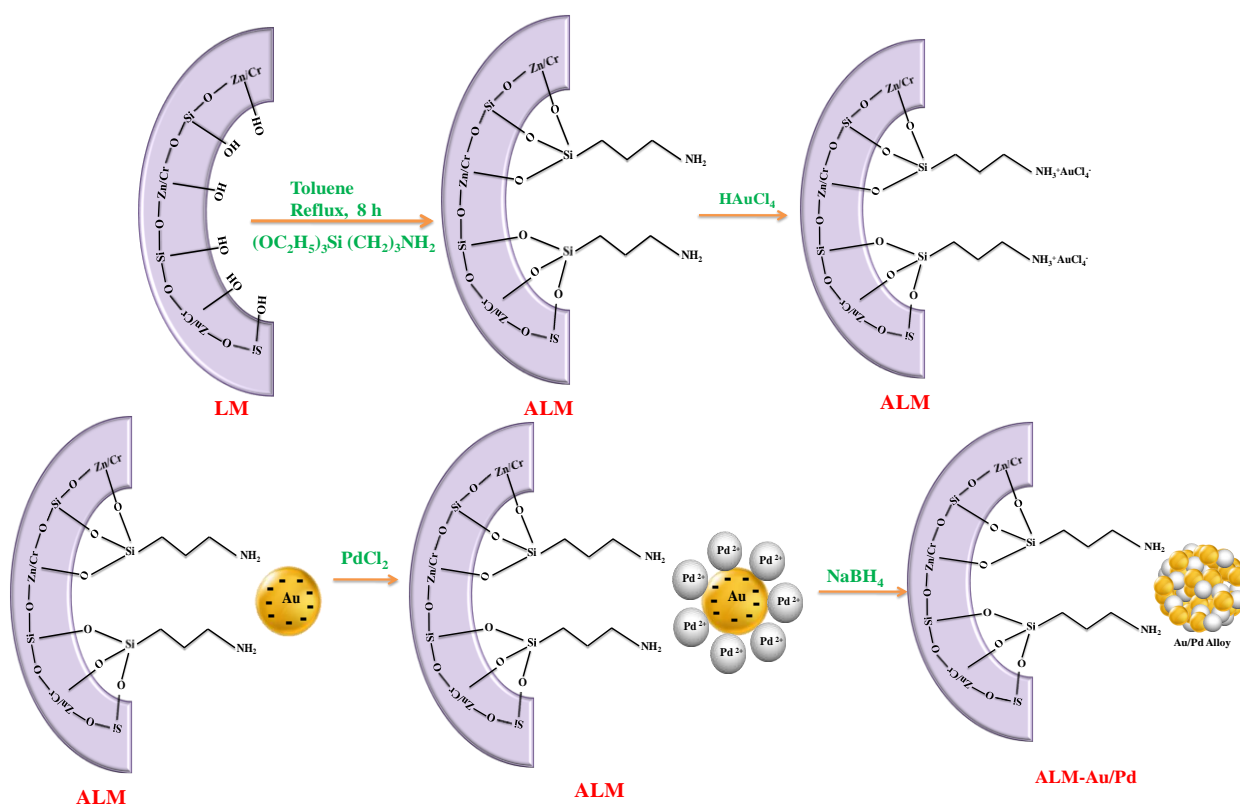
Synthesis of Au/Pd-amine@ ZnCr LDH -MCM-41 (ALM-Au/Pd)

After investigating the photocatalytic activity of all amine functionalised material (AL_{0.2}M, AL_{0.33}M, AL_{0.5}M and ALM) samples, ALM was selected to load noble metal nanoparticles. ALM-Au/Pd catalyst was prepared by reduction impregnation method, with the weight ratio of Au/Pd (1:1). 1 gm of ALM composite was sonicated for 30 min in 20 mL deionised water. To load 1 wt% of both Au and Pd nanoparticles, an estimated amount of HAuCl₄, PdCl₂ and KCl (2 equiv. with respect to PdCl₂,) aqueous solution was added to the above suspension and stirred for 12 h. The solid was centrifuged and washed with deionised water and collected for further use. Then this product was redispersed in 50 mL NaBH₄ solution and continued to stirring for another 2 h. Consequently a dark gray colour mass was obtained. The product was filtered and dried in vacuum. For comparison study, monometal (Au 1 wt%, Pd 1 wt%) loaded ALM nanocomposites were prepared by following the above procedure and denoted as ALM-Au and ALM-Pd.³⁰

Formation mechanism of AuPd alloy on ALM composite

This synthesis procedure was illustrated in Scheme 1 As the pore walls of MCM-41 are covered with residual surface silanol groups and the brucite layers of LDH contain hydroxyl groups, the LM composite can be functionalised with organic moieties (APTES). During functionalisation a covalent bond [represented by an M–O–Si bond (M = Zn,Cr and Si)] was formed through the condensation of APTES molecule and hydroxyl group of LM composite.³¹ After functionalisation, the organic amine groups present on LM surface facilitates the metal ions to uniformly anchor and form noble metal loaded nanohybrids. Bimetallic colloids can readily synthesized by surfactant free co-reduction method utilizing reducing agent NaBH₄. Usually, the metal species having the higher redox potential get reduced first and then the second component get reduced.³² As reduction potential of Pd²⁺ (PdCl₄²⁻/Pd⁰=0.591 vs SHE) is higher than Au³⁺ (HAuCl₄ /Au⁰ = 1.008vs SHE), reduction of HAuCl₄ is occurred first and subsequently PdCl₂ reduced by NaBH₄. The AuCl₄⁻ having negative charge can easily attached to the -NH₂ groups through the coordinate bond. Then, Pd²⁺ ions were supported on Au lattice to form ALM-Au/Pd nanocomposite. Owing to the bond formation between Au³⁺/Pd²⁺ and -NH₂ groups, most of the Au³⁺ and Pd²⁺ are attached to the -NH₂ groups. After the addition of NaBH₄, Au³⁺ and Pd²⁺ were reduced to metallic Au and Pd simultaneously. Owing to the whole charge move from Pd to Au leads to formation of alloy in between Au and Pd metal. Upon alloying, Pd loses s, p electrons and

accepts d-electrons, whereas Au accepts s, p electrons and loses d-electrons resulting coulombic attraction between them.³³ Basically formation of an alloyed bimetallic nanoparticles (Au/Pd) is dependent on following points. (1) metal ions having approximately same redox potentials, metal with comparatively high enthalpies of mixing and nearer atomic size, (2) strength of bonding between two atom must be strong, otherwise segregation is occurred (3) Surface energy is an important factor for mixing of two hetero atom, (4) Charge transfer between less to high electro negative atom facilitate the formation of alloy.³⁴



Scheme 1. Formation mechanism of ALM-Au/Pd.

Materials Characterization

Using Rigaku Miniflex powder diffraction meter along with Cu $K\alpha$ radiation ($\lambda = 1.54 \text{ \AA}$), the powder X-ray diffraction (PXRD) of materials were carried out. The instrument was set at 15 mA with 30 kV and run between the ranges of 5° to 70° at a scan rate of $2^\circ/\text{min}$. The BET surface area was analysed by the multipoint N_2 adsorption–desorption technique using NOVA3000 (Quantachrome GmbH, Germany) instrument at liquid N_2 temperature of 77 K. Prior to analysis, the sample was degassed for 2 h at 80°C under vacuum conditions to remove the physically adsorbed water. Applying the Barrett-Joyner-Halenda (BJH) technique, the pore size distribution and pore volume were calculated. The stretching and bending frequency mode of the materials was measured with the help of Fourier transform

infrared (JASCO FT/IR-4600) within the wavenumber range of 4000–400 cm^{-1} . KBR matrix was used as the reference for measurement of all the samples. X-ray photoelectron spectroscopy (XPS) was measured with a VG Microtech Multilab ESCA 3000 spectrometer. Mg K α X-ray was used as nonmonochromatized source. The C 1s spectra of carbon atom were taken as a reference for the binding energy correction. ZEISS SUPRA55 microscope was used for obtaining scanning electron microscopy (SEM) images. To determine the surface micrographs of sample, high resolution transmission electronic microscopy (JEM-2100F) was used and run at 200 kV accelerating voltage. For preparing the specimen the powder sample was dispersed in ethanol (3 min) after that this suspension was added with drop wise manner on the carbon coated copper grid. The optical absorbance was measured within the wavelength of 200–800 nm and equipped by ultra violet–visible diffuse reflectance spectrophotometer (JASCO-V-750). Boric acid pallet was taken as reference sample. The photoluminescence behaviour of the samples were characterised by JASCO-FP-8300 fluorescence spectrophotometer in which Xenon lamp is the light source. The PL spectra were performed in room temperature at the excitation wavelength of 350 nm. Time resolved photoluminescence (TRPL) spectra, was measured by Edinburg Instrument FLS920 fluorescence spectrometer with multi channel scaling (MCS) module, which equipped with a F290H pulsed Xenon micro second flash lamp.

All the photoelectrochemical measurements were done by potentiostat–galvanostat (IVIUMnSTAT) electrochemical workstation, equipped with 300 wt Xenon lamp as visible light source. The whole system consists of three electrode arrangement, where, Pt and Ag/AgCl electrode and prepared fluorine-doped tin oxide (FTO) were taken as counter and reference and working electrode respectively. FTO was made by electrophoresis deposition method (20 mg of both sample and iodine powder was dispersed in 40 mL acetone then two FTO were positioned within the solution in opposite facing parallel to each other). 0.1M Na₂SO₄ solution was used as electrolyte solution. The Nyquist plot was carried out at 10⁵ Hz to 10¹ Hz at 0 biases. The linear sweep voltammetry (LSV) plots carried out by applying the potential from 0–1.4V at scan rate 20 mV/sec under light irradiation and dark condition. The Mott–Schottky (MS) plot was done at frequency of 500 Hz. The chronoamperometry was performed at potential of 0.8V for 5 min.

Photocatalytic reaction

The photocatalytic activity of the as-synthesized catalysts was examined by selective one pot synthesis of imine through photocatalytic oxidation and reduction of benzyl alcohol and

nitrobenzene respectively. The complete synthesis procedure was implemented as follows: 0.05 gm of material was added into 10 mL acetonitrile containing benzyl alcohol (3mmol) and nitrobenzene (1mmol), and then mixture was illuminated under visible light in an irradiation chamber (BS-02, Germany) for 3h. The mixed suspension was stirred vigorously for 30 min in dark condition before visible light irradiation to maintaining the chemisorptions equilibrium between the substrates and photocatalyst. 250 W medium pressure Hg lamp was equipped as light source and 1M NaNO₂ solution as cut-off filter ($\lambda \geq 420$ nm). The reaction temperature was adjusted at 35⁰-40⁰C by circulating the cold water during the experiment. At the end of reaction the solution mixture was centrifuged to remove the sample particles. Then this resultant reaction solution was qualitatively analysed by gas chromatograph (GC, Thermo scientific Trace 1110) and quantitatively determined with gas chromatography– mass spectrometer (GC–MS, Thermo scientific Trace 1300). Conversion rate of benzyl alcohol and nitrobenzene, yield of benzaldehyde, imine, aniline and the reaction selectivity were calculated by following equations(1-4).

$$\text{Benzyl alcohol or nitrobenzene conversion (\%)} = \left(\frac{C_0 - C_1}{C_0} \right) * 100 \quad (1)$$

$$\text{Benzaldehyde or aniline yield (\%)} = \left(\frac{C_2}{C_0} \right) * 100 \quad (2)$$

$$\text{Imine yield} = \left(\frac{\text{moles of imine compound}}{\text{moles of initial nitrobenzene}} \right) * 100 \quad (3)$$

$$\text{Benzaldehyde, aniline or imine selectivity (\%)} = \left[\frac{C_2}{(C_0 - C_1)} \right] * 100 \quad (4)$$

Here C₀ is the initial concentration of reactants (benzyl alcohol, nitrobenzene), C₁ is the amount of benzyl alcohol and nitrobenzene after photocatalytic reaction whereas C₂ is the concentration of generated benzaldehyde and aniline at the end of reaction. Theoretically the yield of imine is decided by the amount of nitrobenzene taken initially.³⁵

Results and Discussion

PXRD analysis was performed to investigate the structural property, phase purity and crystalline character of the resulting composite materials in comparison to the parent LDH. Figure 1a showed the XRD pattern of LDH, MCM-41 and low angle XRD pattern of MCM-41(inserted). LDH clearly exhibited the characteristic diffraction patterns at 2 θ values of 11.5°, 23.43°, 34.3°, 38.8°, 47.3°, 59.6° and 61.1° corresponding to (003), (006), (012), (015), (018), (110) and (113) basal planes, indicating the formation of crystalline ZnCr LDH with hydroxalcalite-like structure matching with JCPDS (JCPDS: 41-1428).³⁶ Bragg reflections

claimed that LDH have R_{3m} rhombohedral symmetry with several contents of Zn/ Cr octahedron lattice. The basal spacing d_{003} plane indexed as carbonate intercalated LDH close to its value 0.77 nm. By the contribution of the diffraction planes (110) and (003), the lattice parameters $a = 2d_{110}$ and $c = 3d_{003}$ were determined. XRD patterns of MCM-41 (low angle inserted) showed three distinct peaks, (100) diffraction plane indicating the typical mesoporous structure, other two characteristic reflections (110) and (200) having less intense peaks representing the hexagonal periodic long range order lattice of MCM-41.³⁷ A broad peak at 2θ of 23.0° in high angle diffraction of MCM-41 explained the amorphous framework of MCM-41. After the composite formation between LDH and MCM-41, the intensity of all the peaks of LDH drastically decreased (Figure 1b). Especially the d_{003} Bragg's plane of LDH became less intense and broad suggesting a negative influence of MCM-41 on crystallinity of LDH which results in stacking defects and imperfection in the ab plane and along the c-axis of LDH. MCM-41 had a more pronounced effect to control the LDH crystals growth direction, which reveals to poor crystallinity.³⁸ After amine functionalisation the same XRD patterns were maintained indicating the well ordered structural arrangement. Due to lower loading of Au and Pd nanoparticles and good dispersion on the support, the characteristic diffraction patterns of Au and Pd are not prominent. Moreover, overlapping of diffraction patterns of neat LDH and noble metal nanoparticles in case of ALM-Au and ALM-Pd result in the appearance of a broad intense peak at around 2θ value of 38° - 40° . Upon deconvolution, presence of two diffraction patterns confirmed the loading of Au and Pd on ALM support. The inserted XRD image in Figure 1b showed two peak at 38° and at 40° representing (111) basal planes of Au and Pd nanoparticles respectively. However, upon loading bimetallic Au/Pd nanoparticles, a weak broad diffraction peak in between at 2θ of 38° to 40° was observed. Although these two peaks in case of monometallic ALM are very broad, the peak position in case of bimetallic alloyed nanoparticles clearly indicated an intermediate scattering angle (The (111) basal planes of ALM-Au, ALM-Pd and ALM-Au/Pd are deconvoluted and inserted in Fig. 1b). In addition, slight shifted in the diffraction peaks of the bimetallic nanoparticles was observed from ALM-Au to ALM-Pd. This confirmed the formation of Au-Pd alloys nanoparticles in ALM-Au/Pd nanocomposite rather than the simple mixture of bi metal nanoparticles. The Pd nanoparticles entered into the crystal lattice of Au nanoparticles resulting in the formation of alloyed nanoparticles due to slight mismatch in their structure. Au lattice have tendency to capture the Pd lattice, revealed to close interaction between them and helped to produce of Au/Pd alloy.^{39;40} The mean crystallite size of noble metal nanoparticles were calculated using Scherrer formula by considering (111)

peak of ALM-Au, ALM-Pd and ALM-Au/Pd nanocomposite with the help of full width at half maximum. The crystallite size of Au, Pd and Au/Pd alloy nanoparticles were found to be 3.0 nm, 1.97 nm and 2.1 nm respectively. The decrease in the crystallite size of the bimetallic alloyed nanoparticles in comparison to monometallic Au may be due to difference in the velocity of growth of the individual monometallic nanoparticles. As the ionization potential of Pd nanoparticles (8.33 eV) is lower than the ionization potential of Au nanoparticles (9.22 eV), incorporation of Pd inhibits the growth of bimetallic alloyed nanoparticles.⁴¹ The XRD results demonstrated the successful creation of Au/Pd alloy nanoparticles on the surface of ALM nanocomposite and produced a better photocatalyst for organic transformation reaction. To determine the mesoporous behaviour and textural property of the catalysts, N₂ adsorption–desorption technique is a common method. This study provides information about the approximate pore diameter, specific surface area, and pore volume etc. Figure 1c and 1d showed the N₂ isotherm and pore size distribution plot of LDH (inserted) LM, ALM and ALM-Au/Pd. Table 1 summarises the textural specification of the samples obtained from N₂ adsorption/desorption isotherms analysis. By using BET and BJH method, specific surface area and pore size of materials were calculated. According to the IUPAC classification, the shape of all the graphs suggests, type IV isotherm which confirms the mesoporous nature of the material. During N₂ adsorption–desorption, a narrow hysteresis loop (type H3) at the relative vapour pressure range from 0.4–0.8 was obtained.⁴² This confirms presence of aggregated plate-like mesoporous material, giving rise to irregular pores with non uniform size. Maximum adsorption was observed at relative pressure of $P/P^0 = 1$. According to our previous literature, the obtaining specific surface area and pore size of MCM-41 was found to be 878 m²/g and 3.4 nm respectively.³⁷ As shown in Table 1, neat LDH showed the surface area of 28.7 m²/g. The pore size distributions were relatively narrow and found to be 6.14 nm. After the modification of LDH with MCM-41 the surface area (305.7 m²/g) was drastically decreased than MCM-41 but significantly increased from LDH material, this information suggested that the active sites of LDH were uniformly distributed over the MCM-41 support and behaves as good base catalyst. The homologous structure of LM was due to the uniform nucleation and growth in an end-face way.³⁸ After the functionalisation of APTES on the surface of LM, the surface area was also remarkably decreased. This reason was associated with the bonding of organic moiety APTES groups with Si-OH and Zn/Cr-OH in the framework of ALM sample revealed surface coverage of the parent material.⁴³ Additionally, the introduction of Au/Pd alloy to the ALM surface resulted to some extent of pore blocking and decreased the surface area and pore volume also but there is an increase in number of

active sites which is beneficial for photocatalytic activity. The pore size distribution of all samples was calculated to be 3-7 nm which suggests all the parent and nanocomposites were in mesoporous range.

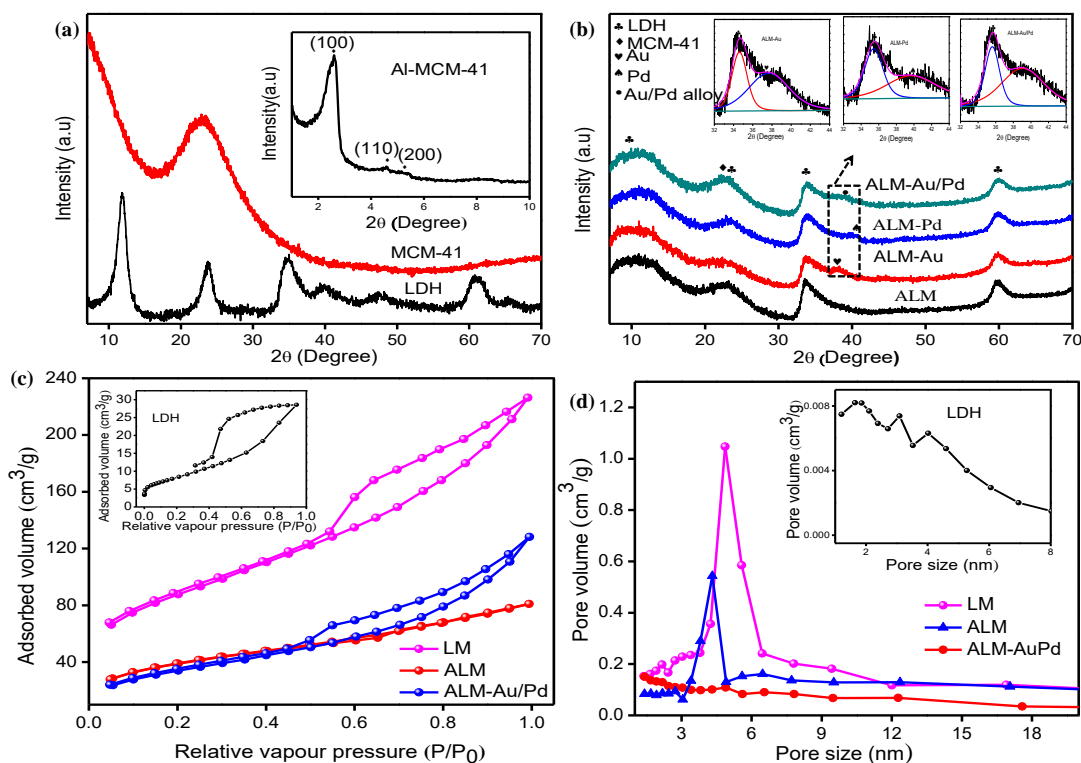


Fig. 1 XRD patterns of LDH and MCM-41 (a), ALM, ALM-Au, ALM-Pd and ALM-Au/Pd (b), N₂ adsorption-desorption isotherm (c) and pores size distribution (d) of LDH (inserted), LM ALM and ALM-Au/Pd.

Table 1 textural property of MCM-41, LDH, LM, ALM and ALM-Au/Pd

Samples	Specific surface area (m ² /g)	Pore Size (nm)	Pore volume (cm ³ /g)
MCM-41	878	3.4	0.65
LDH	28.7	1.64	0.04
LM	305.7	4.59	0.35
ALM	136.7	4.31	0.20
ALM-AuPd	124.4	4.7	0.12

The surface micrographs of ALM-Au/Pd were investigated by SEM analysis. Fig. S1 depicted the image of LDH, ALM and ALM-Au/Pd nanocomposite. Pure LDH was appeared as large assemblage of flaky-sheet-array lying on top of one another owing to hydrothermal compound prepared by co-precipitation method.^{36,44} As shown in Figure S2b, after functionalisation of ALM by organic moiety followed by heterostructure formation between

MCM-41 and LDH, displayed irregular shape with loosely agglomerated particles. However, the immobilisation of noble metal particles on the surface of ALM is not prominent owing to the uniform anchored and small particle size of metal particles. The incorporation of Au/Pd alloy onto ALM keeps the structure intact.

The actual microstructure, particle size and nature of distribution of bimetallic alloyed nanoparticles was further investigated by TEM and HRTEM analysis of the representative LDH, ALM and ALM-Au/Pd sample. From the TEM image shown in Fig. 2a, LDHs are found to be composed of crystallites with typical plate like morphology having irregular hexagonal shapes and the particle size within the nanometric range.³⁶ The TEM image of ALM nanocomposite (Fig. 2b) clearly suggests mesoporous morphology in which a good interaction exist between LDH with the framework of MCM-41 in consistency with FTIR and N₂ adsorption-desorption study. It can be found that large quantities of small spherical bimetallic alloyed Au/Pd nanoparticles were greatly dispersed and embedded on the ALM support in highly homogeneous manner. The corresponding particle size distribution in ALM-Au/Pd was calculated, by measuring more than 200 particles from different regions. The size distribution is narrow, with average particle size found to be about 3-4 nm (Fig. 2c and d). ALM-Au/Pd images indicate Au/Pd alloy nanostructures were encapsulated by the mesochannels of ALM nanocomposite. High-resolution TEM (HRTEM) is essential for metal nanoparticle to determine not only the shape and particle size but also gives information about crystallography phase. Moreover, when Au/Pd bimetallic nanoparticle get alloyed at any molar ratio, the face centered cubic (fcc) lattice structure was arisen.⁴⁵ Further, the HRTEM image (Fig. 2e) of a single alloyed NP results lattice fringes with an intermediate interplanar basal spacing of about 0.230 nm, which is slightly lower than the lattice spacing of metallic Au ($d_{111}=0.235$ nm) but higher than the metallic Pd lattice spacing ($d_{111}=0.225$ nm). This change in interplanar lattice spacing value may result both geometric and electronic effects, which in turn modulate the chemical and catalytic properties of the nanocomposite showing enhanced activity. These observations clearly confirms the formation of bimetallic alloyed Au/Pd nanoparticles and segregated monometallic nanoparticles with preferentially exposed (111) plane.^{45,46} The polycrystalline nature of ALM-Au/Pd sample was confirmed by selected-area electron diffraction (SAED) pattern (Fig. 2f). The rings are related to (006) and (110) plane of LDH with the (111) plane for the Au/Pd alloy nanoparticles, in accordance with the XRD results. EDX technique is one of the most useful methods for evaluating the constitution of bimetallic nanoparticles, to observe the local metal compositions and

distribution of other element. Fig. 2g represents the homogeneous dispersion all elements in the ALM-Au/Pd materials.

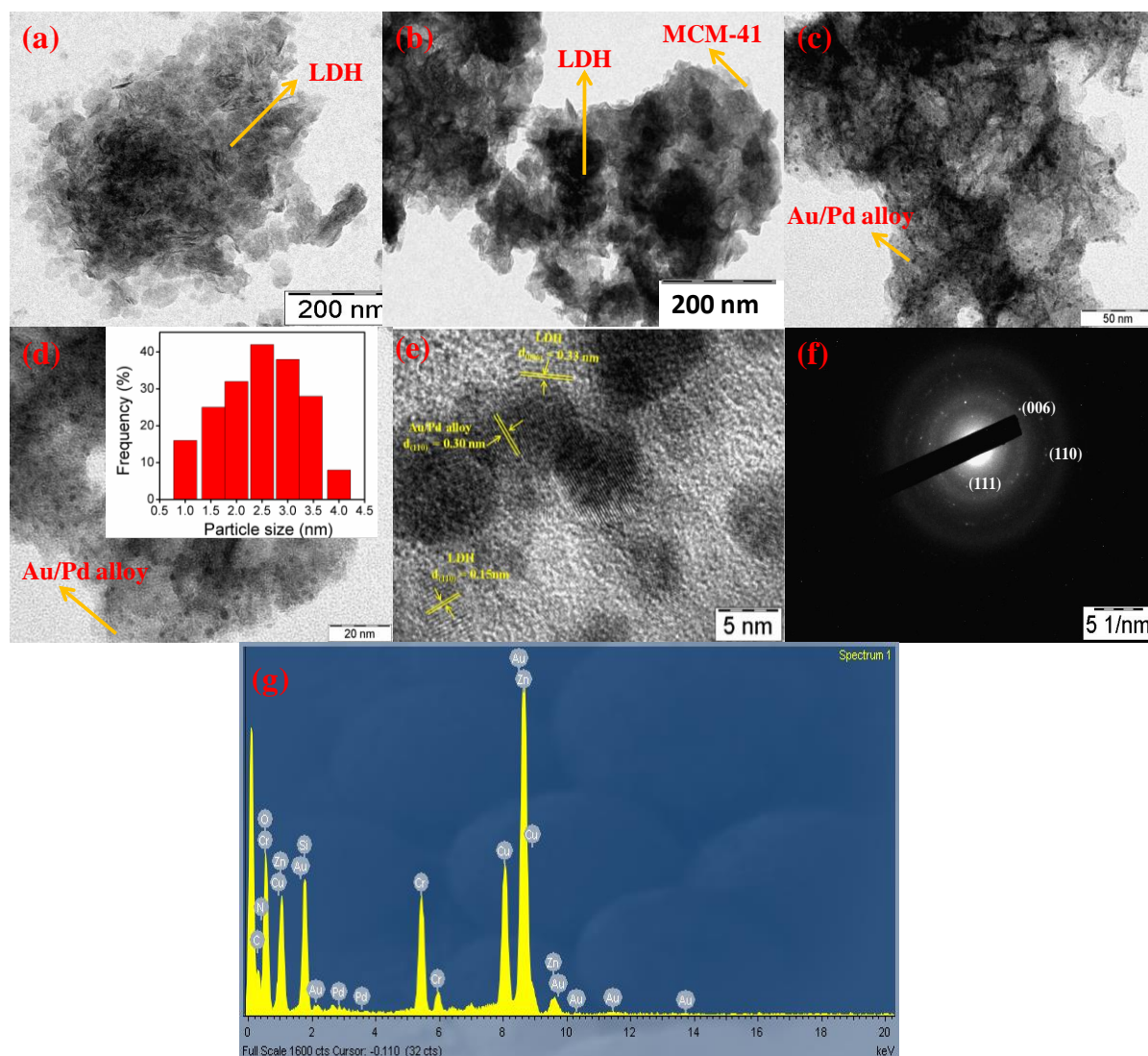


Fig. 2 TEM images of (a) LDH (b) ALM, (c) and (d) ALM-Au/Pd. HRTEM images of (e) lattice fringes, (f) SAED pattern and (g) EDS over the ALM-Au/Pd.

FTIR spectra were measured to assure the existence of bonding and the influence of functional group in the as synthesized material. Fig. 3 showed the FTIR spectra of LDH, LM, ALM, ALM-Au, ALM-Pd and ALM-Au/Pd nanocomposites. A broad spectrum was formed at $3300\text{--}3600\text{ cm}^{-1}$ in the case of all samples due to the stretching vibration of -NH_2 group (APTES molecule), which was overlapped with the surface hydroxyl groups, intercalated water molecule of LDH and also hydroxyl group of MCM-41.^{25,37} The broadness of the peak illustrates H-bonding in a large range of vibrational frequency. After the composite formation between LDH and MCM-41, the broadness of -NH_2 and -OH stretching slightly decreased due to the strong interaction between APTES, LDH and MCM-41. All materials showed a

weak band at 1630-1650 cm^{-1} for H-O-H bending vibration of water molecule. Whereas the symmetric and asymmetric stretching mode of carbonate anion in inter gallery space were appeared at 1493 cm^{-1} and 1370 cm^{-1} respectively in the case of LDH.³⁶ After composite formation, the width of carbonate stretching vibration mode suddenly decreased because MCM-41 greatly affects the intercalated carbonate ion which is consistent with XRD results. All the LDH based composite except MCM-41 showed a series of the bands at low frequency region due to lattice vibration and deformation modes of Zn/Cr-OH (660 cm^{-1}) and Zn-O-Cr (585, 500 cm^{-1}) bond. A characteristic band at 1033–1245 cm^{-1} was due to the Si–O stretching vibration of Si–O–Si structure present in the MCM-41 and in all the composites (except LDH). The existence of spectrum at 966 cm^{-1} and 790 cm^{-1} were attributed to Si-Zn/Cr-O-Si and Si-Zn/Cr--OH vibration band respectively, revealing formation of a composite between LDH and MCM-41.⁴⁷ Presence of N-H bending (750 cm^{-1}), $-\text{NH}_2$ symmetric vibration (1532 cm^{-1}) and $-\text{CH}_2$ group asymmetric vibration (2940 cm^{-1}) of propyl chain in APTES in case of all the composite materials (ALM, ALM-Au, ALM-Pd and ALM-Au/Pd) confirms favourable grafting of organic moiety on the surface of ALM.⁴⁸ Even after amine functionalization and coupling with MCM-41, the corresponding vibration modes were maintained confirming good coordination between LDH and MCM-41. After loading of noble metal nanoparticles there was no distinct variation, indicating the Au/Pd nanoparticle deposition has not altered the structure of ALM. All observed bands were become sharper and clear after loading metal nanoparticles which was in good agreement with XRD analysis.

X-ray photoelectron spectroscopy (XPS) is a surface responsive technique, which not only gives information about of the atomic composition on the surface of a catalyst but also the oxidation states regarding to the binding energy of the inner shell electrons. The details information with respect to the bonding nature of atoms in the ALM-Au/Pd monohybrids in comparison to its pristine LDH counterpart was measured by deconvolution of XPS peaks of each element using CASA XPS software. In case of pure LDH, the Zn 2p and Cr 2p core lines split into four peaks of Zn 2p_{3/2} (1022.0 eV), Zn 2p_{1/2} (1045.0 eV), Cr 2p_{3/2} (577.7 eV) and Cr 2p_{1/2} (587.1 eV) shown in Fig. 4a and 4b, suggesting the existence of Zn(OH)₂ and Cr(OH)₃ in the positive sheet of LDH.⁴⁹ Whereas, the peaks of Zn 2p and Cr 2p in case of ALM-Au/Pd nanocomposite were appeared at slightly higher binding energy (Zn 2p_{3/2}-1022.4 eV, Zn 2p_{1/2}-1045.5 eV, Cr 2p_{3/2}-578.1 eV and Cr 2p_{1/2}-587.6 eV) in compared to pristine LDH. Additionally the spin orbit state of Si 2p in neat SiO₂ was observed at binding

energy of 103.2-103.7 eV suggesting the +4 oxidation state of Si.⁵⁰ But in the present study, after the composite formation with LDH and loaded with Au/Pd alloy nanoparticles (ALM-Au/Pd), the binding energy of Si 2p was also shifted to higher value of 103.8 eV in comparison to the reported value shown in Fig. 4e. The positive shifting in binding energies suggests reduction in the electron density around Zn, Cr, and Si in the ALM-Au/pd due to transfer of electron from ALM to Au/Pd alloy. As depicted in Fig. 4d, the XPS spectrum of C 1s in pure LDH showed two peaks at binding energy of 284.9 eV and 288.8 eV attributed for reference carbon and carbonate anion present in intergallery space of LDH structure respectively, but in case of ALM-Au/Pd, three peaks of C1s spectra were observed at the binding energy of 284.9 eV, 286.5 eV and 291.5 eV for reference carbon, C-N bonding and intergallery carbonate anion respectively. The blue shift in binding energy of C 1s peak corresponding to C-N bonding and carbonate anion suggests a strong interaction exhibits between LDH and MCM-41. This C-N bonding peak indicates the successful grafting of APTES group on LM surface.⁵¹ As shown in Fig. 4c, the core level peaks of the O 1s spectrum in neat LDH and ALM-Au/Pd were deconvoluted. Upon deconvolution two peaks corresponding to binding energy of 531.5 eV and 532.2 eV were obtained due to hydroxide group of brucite layer and intercalated carbonate anion in LDH respectively.⁴⁹ After functionalisation of LM with APTES, the O 1s spectrum corresponding to hydroxide group was shifted towards positive binding energy (531.9 eV).⁵² The increased in binding energy illustrates a strong coupling of covalent bond between -OH groups of ALM and -OC₂H₅ group of APTES. Fig. 4f showed the N 1s spectrum of ALM-Au/Pd sample. The splitting of N 1s spectrum into amino (-NH₂) and ammonium (-NH₃⁺) groups were appeared at the binding energy of 399.9 eV and 401.3 eV respectively.⁵³ The presence shoulder peak of ammonium groups indicates the decrease of electron cloud density over N atom, suggests a chemical bond established between Au/Pd alloy to N atom. The amino group have capable to donate electrons into the transition metal owing to its electron pairs on N atom and in other way the Au/Pd alloy have empty energy orbit for accepting electron from N atom, which results a strong coordinative bond formation between N atom and Au/Pd alloy.²⁵

The Au 4f and Pd 3d core level spectra in ALM-Au/Pd sample were shown in Fig 4g and 4h. The four strong peaks of Au 4f (4f_{7/2} and 4f_{5/2}) and Pd 3d (3d_{5/2} and 3d_{3/2}) were appeared at binding energy of 83.88 eV, 87.49 eV, 335.36 eV and 340.64 eV respectively in the case of single metal loaded LDH composite.^{22,54} In contrast, after the formation of alloy between Au and Pd in ALM-Au/Pd nanocomposite, the binding energy of Au 4f was shifted towards negative value (4f_{7/2}- 83.7 eV and 4f_{5/2}- 87.4 eV) whereas the spectrum of Pd 3d situated at

higher binding energy ($3d_{5/2}$ -335.7 eV and $3d_{3/2}$ -341.5 eV) with relative to monometallic reported value. This peak shifting indicates a close electronic interaction between Au and Pd in the created alloyed nanoparticle. In other words the electron mobility takes place from the smaller electronegativity of Pd (2.2) to larger electronegativity of Au (2.4).²⁴ That was also satisfied for formation of Au/Pd alloy structure. Consequently electron cloud around Au nucleus increases while the electron concentration decreases around Pd nucleus.³⁴ Greater the electron density leads to increase the screening effect of Au nanoparticle and resulted negative shift in binding energy. The survey scan of XPS spectra was represented in Fig.4i. From the XPS results, conclusively it can be said that the lower binding energy of Au/Pd alloy and higher binding energy of Zn, Cr, Si suggests an efficient composite formation between ALM and Au/Pd alloy nanoparticle in which the charge heterogeneity on alloy surface enhance the photocatalytic organic conversion process.

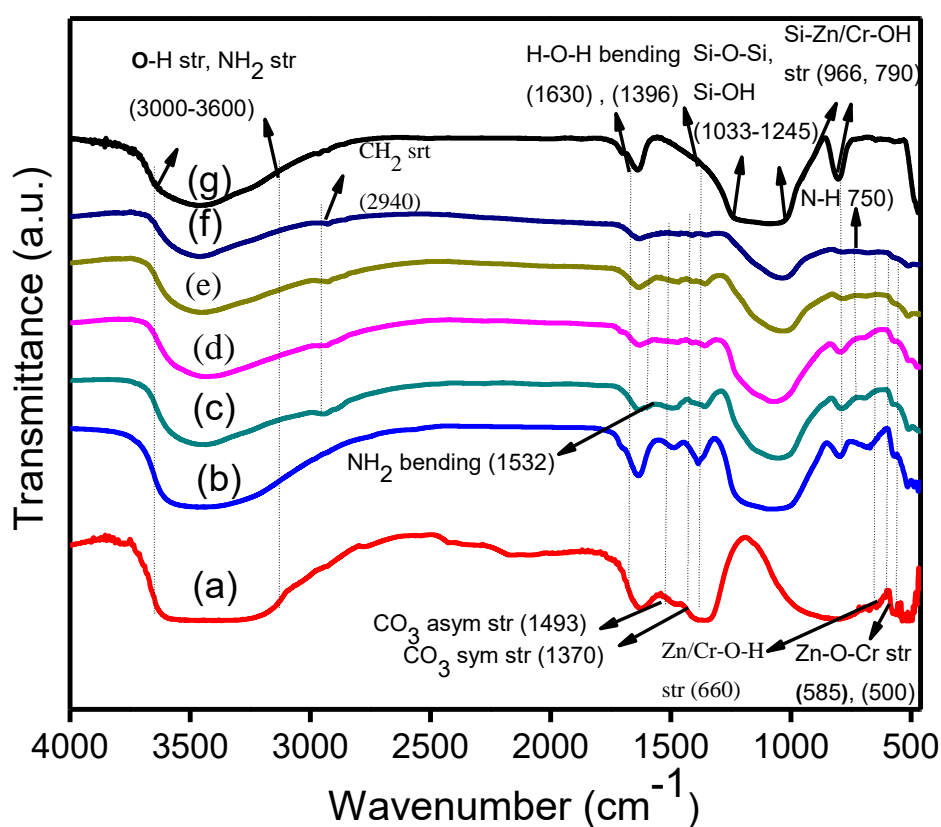


Fig. 3 FTIR spectra of (a) LDH (b) LM (c) ALM (d) ALM-Pd (e) ALM-Au (f) ALM-Au/Pd (g) MCM-41

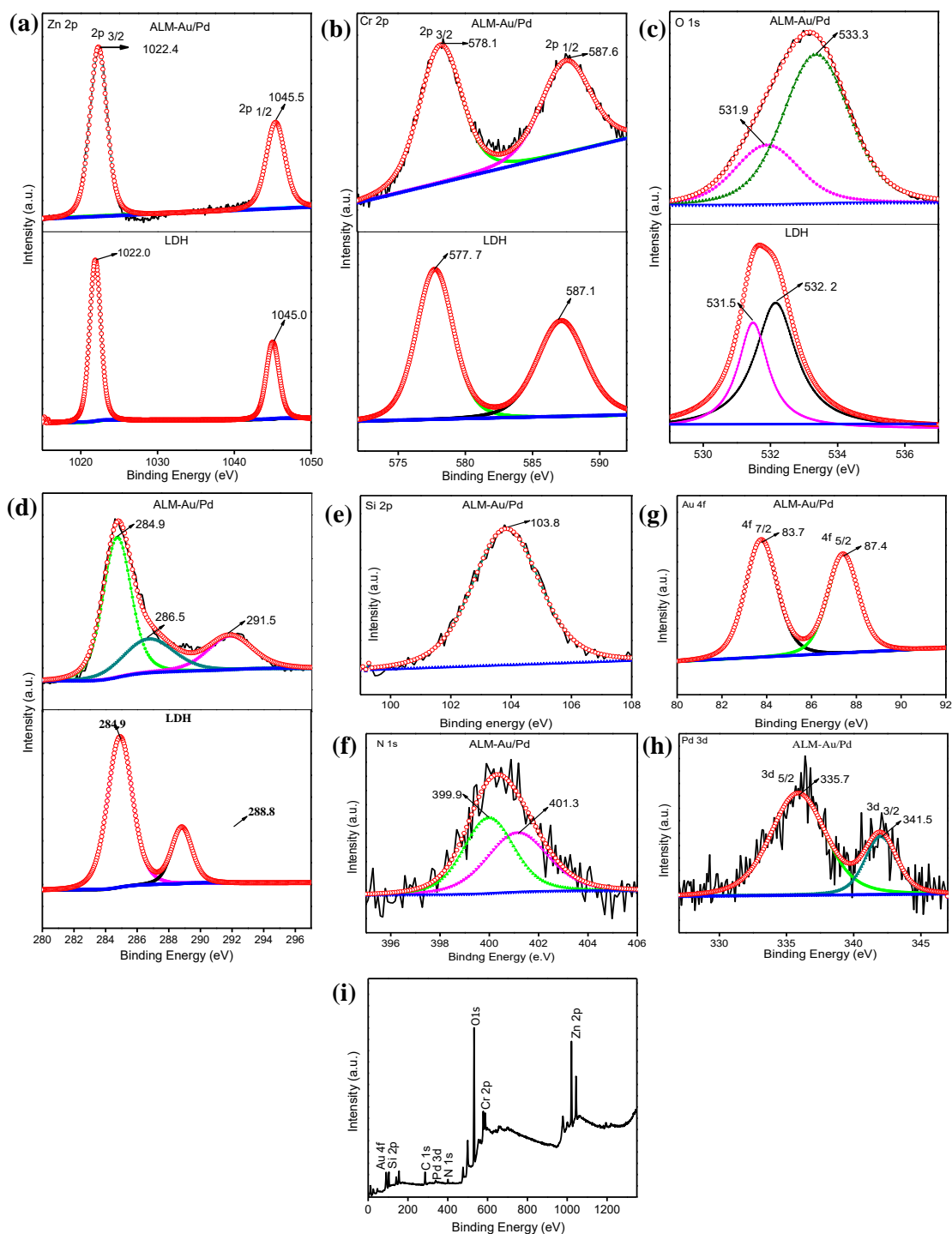


Fig. 4 High resolution deconvoluted XPS spectra of LDH and ALM-Au/Pd.

The opto-electronic behaviour of the as prepared samples were analysed by UV-Visible absorption spectrum and represented in Fig. 5. It was seen that, after the formation of ALM and after loading noble metal nanoparticles, absorption edge shifts towards a longer wavelength, indicating enhanced light absorption and consequently improved photocatalytic activity in the visible region. The absorption edge of LDH was gradually increased towards

higher wavelength with loading of monometallic noble metal nanoparticles to bimetallic alloyed noble metal nanoparticles. Neat LDH showed intrinsic broad absorption bands in 200–300 nm regions due to ligand to metal charge transfer (LMCT) from the O-2p orbital to the Zn-4s and Cr-3deg orbital. In the visible light region, the absorption peaks at 413 and 570 nm attribute to the $4A_{2g} \rightarrow 4T_{1g}(F)$ and $4A_{2g} \rightarrow 4T_{2g}(F)$ d-d transitions of the Cr^{3+} ions, respectively.⁵⁵ After loading of Au nanoparticles, ALM-Au should show LSPR peak around 520 nm, however in this case a broad absorption peak was appeared as the LSPR peak overlaps with the MMCT band of ALM. Moreover, upon loading Pd nanoparticles the LSPR band of Au nanoparticles change and a broad weak characteristic peak was observed at about 520-570 nm (ALM-Au/Pd).²² The combination of Au atoms with Pd atoms, results to change in the colour of the sample from purple to gray. It has been reported that incorporation of Pd into the crystal lattice of Au changes the crystal structure of Au. This phenomenon was based on previous observations, that the presence of a metal atom (group 10) with d^8s^2 configuration in bimetallic alloyed nanoparticles suppresses the LSPR energy of a metal atom (group 10) with $d^{10}s^2$ configuration.⁴¹ The band-gap energy of LDH can be calculated by fitting the absorption data with the Kubelka–Munk equation and Tauc's plot (Fig. S2). The neat LDH displayed direct allowed transitions and band-gap energy value was found to be 2.5. This band gap of LDH indicates ability of harvesting visible light photons.⁵⁶

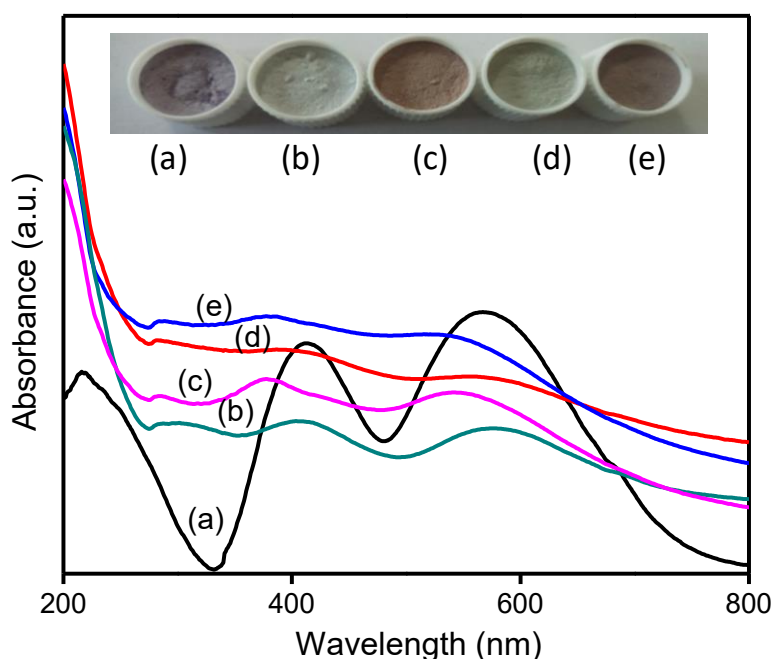


Fig. 5 UV-Vis diffuse reflectance spectra of (a) LDH (b) ALM (c) ALM-Au (d) ALM-Pd (e) ALM-Au/Pd

Photocatalytic activity towards one pot synthesis of Imine from benzyl alcohol and nitrobenzene

At first the photocatalytic activity of the amine functionalised materials (AL_{0.2}M, AL_{0.33}M, AL_{0.5}M and ALM) were performed for selective photoconversion of benzyl alcohol to benzaldehyde under visible light irradiation ($\lambda \geq 420$ nm) (Table S1). ALM (weight ratio between LDH to MCM-41 is 1:1) showed better conversion efficiency of benzyl alcohol (48.7%) with higher yield (46) and selectivity (88%) in compared to other materials due to the higher concentration of LDH makes available of a large number of active sites for photocatalytic reaction. To again improve the photocatalytic organic conversion of the ALM photocatalysts, mono metal (Au, Pd) and bimetal (Au/Pd) nanoparticles were loaded into it. Fig. 6a represents benzyl alcohol conversion, yield and selectivity towards benzyldehyde over all the prepared samples (MCM-41, LDH, ALM, ALM-Au, ALM-Pd and ALM-Au/Pd). It was clearly seen that the rate of conversion and yield was increased from MCM-41 to ALM-Au/Pd nanocomposite. For pure MCM-41, a low rate of conversion (10.3%) and yield (8%) was achieved. The conversion and yield was found to be 42 % and 40 %, respectively in the case of pure LDH. After the functionalisation of APTES on LM composite, the yield and conversion were increased to 46% and 48.7% respectively. Furthermore, the noble metal loading enhanced the photoconversion ability of LDH, the ALM-Pd (66% yield) and ALM-Au (76.2% yield) showed the conversion of 68.9% and 81% respectively. The loading of bimetal significantly increased the conversion and yield than individual monometal nanocomposite, and parent catalysts. ALM-Au/Pd showed the highest conversion (92%) and yield (90%) of benzyl alcohol to benzaldehyde. The selectivity of oxidative product over all catalysts (except MCM-41) was higher than 85%.

Tandem photocatalytic reaction was carried out for the synthesis of imine from benzyl alcohol and nitrobenzene conversion over all samples under visible light illumination ($\lambda \geq 420$ nm). As shown in Fig. 6b, pure MCM-41 showed a negligible yield of imine (3.9%) with less conversion of benzyl alcohol and nitrobenzene than all catalysts owing to its non-sensitive light response.³⁷ In bare LDH, the yields of imine are very low (22%), and the benzyl alcohol (48%) nitrobenzene (53.1%) conversions are also not significant. This suggests that LDH is less active material for imine synthesis due to its low capacity of photoinduced charge pair separation. Reactants and intermediates formed during the condensation may also block the active sites of LDH. The ALM nanocomposite converted almost half of benzyl alcohol (56.3%) nitrobenzene (628%), but their imine yield was only 31%. This indicates, condensation of benzaldehyde with aniline did not occur efficiently on

ALM surface. The imine yield over all catalysts was depicted in the following sequence: MCM-41 (3.9%) < LDH (22%) < ALM (31%) < ALM-Pd (47.6%) < ALM-Au (51.3%) < ALM-Au/Pd (68%). The introduction of noble metal onto the ALM surface enhanced the photoconversion activity. The plasmonic metal nanoparticle possesses LSPR effect and efficiently harvests photon energy owing to its intense and broad absorption spectra over the whole visible spectrum. The sample ALM-Au/Pd nanocomposite promoted complete reaction of nitrobenzene (99%) and benzyl alcohol (96%) with the formation of very high yield and selectivity of imine than monometal composite. Upon alloy formation between Au and Pd, the charge distribution take place between these two metal leads to develop a surface electronic heterogeneity which enhance the interaction between organic substrates and alloy surface.¹³ This facilitates more active sites for the improved photocatalytic organic conversion reaction. The synergetic interaction between Au/Pd alloy nanostructure and ALM naocomposite enhance the production of imine which proceeds energetically by the successive coupling of the photo-produced benzaldehyde and aniline on the ALM-Au/Pd surface. Fig. 6a, 6b and Table S2 represents the conversions, yields and selectivities of all reactants and products over all samples. To get more information about imine synthesis, the reaction was carried out under dark condition. As shown in Fig. S3 a negligible amount of yield (imine) was obtained over all the catalysts. This indicates that the one-pot condensation reaction of benzyl alcohol and nitrobenzene over the ALM-Au/Pd was a photocatalytic process.

Fig. 6b and 6c summarizes the time-dependent change in the amounts of reactants and products during the photocatalytic one-pot condensation reaction with LDH and ALM-Au/Pd. In the first stage, benzaldehyde and aniline were obtained, along with reduction in the concentration of benzyl alcohol and nitrobenzene. With an increased in light illumination time, the amount of aniline gradually increased up to 1 h. After 1 h, the imine formation improved with reducing the aniline quantity. Subsequently after 3 h of light irradiation, approximately maximum amount of the nitrobenzene (99%) was converted to imine (68%), with the generation of benzaldehyde. This is fully in agreement with the following equations (8-12). The photocatalytic one-pot synthesis of imine is quite impressive over ALM-Au/Pd nanocomposite. In less time, a high yield of imine was obtained in compared to other semiconductor based photocatalyst documented in Table 2.

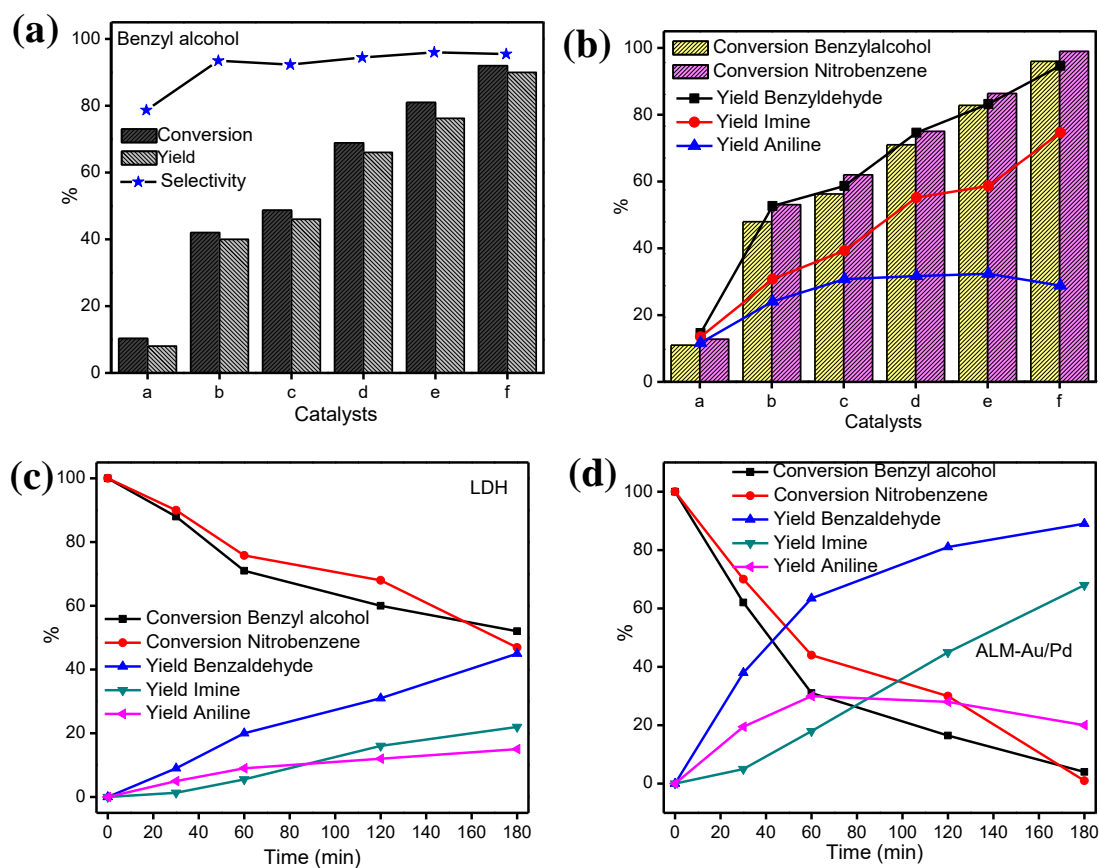


Fig. 6 (a) Photocatalytic benzyl alcohol oxidation of all catalyst [(a)MCM-41 (b)LDH (C)ALM (d)ALM-Pd (e)ALM-Au (f)ALM-Au/Pd] (b) photocatalytic one-pot imine synthesis from benzyl alcohol and nitrobenzene [(a)MCM-41(b)LDH (C)ALM (d)ALM-Pd (e)ALM-Au (f)ALM-Au/Pd]. Time-dependent change in the reactants and products amounts during the photoconversion of benzyl alcohol and nitrobenzene with (c) LDH (d) ALM-Au/Pd.

Table 2 photocatalytic one-pot imine synthesis over different catalysts

Photocatalysts	Substrates	Yield of Product (imine)	Reactions condition	references
CdS(15%)-TiO ₂	Benzyl alcohol(150 μ mol) nitrobenzene (50 μ mol)	>99%	catalyst (10 mg), solvent(hexane 5.0 mL), blue LED light, (λ >420 nm) at room temperature, N ₂ , times: 12 h.	57
P25 TiO ₂	Benzyl alcohol (5 ml) nitrobenzene (0.05mmol)	92%	catalyst (5 mg), 2 kW Xe lamp (λ >300 nm), at room temperature, N ₂ , times:10h	7

Pt(0.3)@TiO ₂	Benzyl alcohol (5 mL), aniline(10 mmol)	97%	catalyst (5 mg), light ($\lambda > 300$ nm), at room temperature, N ₂ , time : 12 h.	58
Cd _{0.78} Zn _{0.22} S	Benzyl alcohol (2.55 mol/L), nitrobenzene (8.5 mol/L)	36.8%	catalyst (80 mg) solvent (BTF, 15 mL), 300 wt Xenon lamp ($\lambda > 420$ nm), at 50°C, N ₂ , time:2h	35
ALM-Au/Pd (present research)	Benzyl alcohol (6 mmol), nitrobenzene (1 mmol)	78%	catalyst (50 mg) solvent (acetonitrile, 10 mL), 250 wt medium pressure Hg lamp($\lambda \geq 420$ nm), time: 3h	

Evidences in support of mechanistic approach for the enhanced photocatalytic organic conversion over ALM-Au/Pd nanocomposite

PL spectroscopy is a kind of powerful and non-destructive technique for characterising the quality of semiconducting materials for elucidating the radiative recombination of charge carriers. PL emission peak is useful in quantifying the impurity content of a material, optical emission efficiencies, composition of the material (alloy composition), and gives idea about localized defect levels generated in a semiconducting material. Fig. 7a represents (LDH was inserted) the PL emission spectra of all synthesized material under an excited wave length of 350 nm. A strong emission peak at 430–450 nm was observed owing to the radiative recombination of localized surface trapped charge pairs of LDH. The presence of weak band at 470 nm corresponds to the band-to-band emission peak of LDH. Moreover the less intense peaks at about 500 nm may be due to the surface defect sites in the material.⁵⁵ There is a drastic decrease in PL intensity in case of bimetallic alloyed ALM composite in comparison to neat LDH, ALM and monometallic composites indicating a significant depression of electron-hole recombination. Generally a reduced PL intensity usually suggests a better separation and transportation efficiency of photoinduced charge carriers. The Au/Pd alloy heterostructure on the ALM surface successfully inhibit the recombination rate of photoinduced charge pairs of LDH by the effect of efficient charge migration in good agreement with the photocatalytic activity.

Further to explain the possible charge transfer dynamics, the TRPL study of the samples (LDH, ALM and ALM-Au/Pd) were carried out as displayed in Fig. 8b. TRPL spectroscopy

helps to describe the increase in life time of the charge carriers in ALM-Au/Pd nanocomposite and decay time of the pure LDH and ALM sample. The different charge pair recombination mechanisms are the function of different PL decay lifetimes of the photocatalysts. The TRPL of the samples was carried at 350 nm as the excitation source. The depicted plots have been fitted with bi-exponential decay functions which expressed by the following equation (equ-5).⁵⁹

$$I(t) = A_1 e^{-\frac{t}{\tau_1}} + A_2 e^{-\frac{t}{\tau_2}} \quad (5)$$

Where τ_1 and τ_2 ($\tau_1 < \tau_2$) are represented by two decay lifetimes of faster and slower component respectively with the corresponding A_1 and A_2 are the PL amplitudes. The τ_1 is originated due to direct generation of charge pairs and τ_2 initiates from the direct formation of self quenched excitation electrons. The average intensity lifetime of both the materials were estimated by making an overall comparison of the emission decay behaviour. Average lifetime (τ) was determined taking the following equation (equ-6).

$$\tau = \frac{A_1 \tau_1^2 + A_2 \tau_2^2}{A_1 \tau_1 + A_2 \tau_2} \quad (6)$$

The bi-exponential decay kinetics is associated with defect level emission from a charge pair recombination of a localized excitation. The calculated average life times of LDH (10.6 μ s), ALM (14.6 μ s) and ALM-Au/Pd (16.2 μ s) were shown in Table 3. Increased average life time in case of AML-Au/Pd nanocomposite suggests efficient transfer of photo excited electron-hole between Au/Pd alloys to ALM with decreasing radiative recombination. This indicates reduction in the recombination probability of localised excitation and subsequently a more number of photo induced electrons and hole are made available to participate in the photocatalytic organic conversion reactions.

Further to explore the electrode reaction kinetics and interfacial charge transfer process, electrochemical impedance spectroscopy (EIS) of all the synthesised catalyst was carried out to monitor the conductivity of the electrode surface after modification. In the photocatalytic process, the interface charge separation ability of the photoinduced charge carriers is an important factor and it can be measured by Nyquist plot. The resulted Nyquist plot as displayed in Fig. 8c was found to consist of a primary semicircular portion to examine the charge transfer resistance. The smaller diameter of impedance arc indicates lower the charge transfer resistance offered by the electrode and more is the conductivity. As shown in the Fig. 8c, the order of the semicircle diameter was LDH (388 Ω) < ALM (150 Ω) < ALM-Pd (58

Ω) < ALM-Pd (50 Ω) < ALM-Au/Pd (46 Ω). Apparently the decreased trend in the diameter of semicircles explains greatly enhanced photocatalytic activity of ALM-Au/Pd. After loading Au/Pd alloy nanoparticles as the solution/electrolyte resistance decreases, the conductivity increases effectively to support the activity. Actually the smallest arc of ALM-Au/Pd nanocomposite than all materials suggested the developed surface charge heterogeneity on the Au/Pd alloy surface retards the high interfacial charge transfer resistance, resulted to the rich electronic and ionic conductivity of materials. The linear portion in the Nyquist plot is the Warburg impedance (W_s) represents the ion diffusion process in the electrolyte supporting the photocurrent response.⁶⁰ The lowest Warburg impedance in case of ALM-Au/Pd in comparison to neat counterparts and monometal nanocomposite confirmed effective ion diffusion in good agreement with the photocatalytic organic transformation.

Based on the results of the steady state PL spectra, TRPL and EIS measurements, it can be concluded that the modification of small amount of Au/Pd alloy on the ALM surface can efficiently separate the recombination property of photo induced charge carriers in ALM and effectively accelerates the visible light conversion efficiency. That's why ALM-Au/Pd nanocomposite showed best photo organic transformation activity.

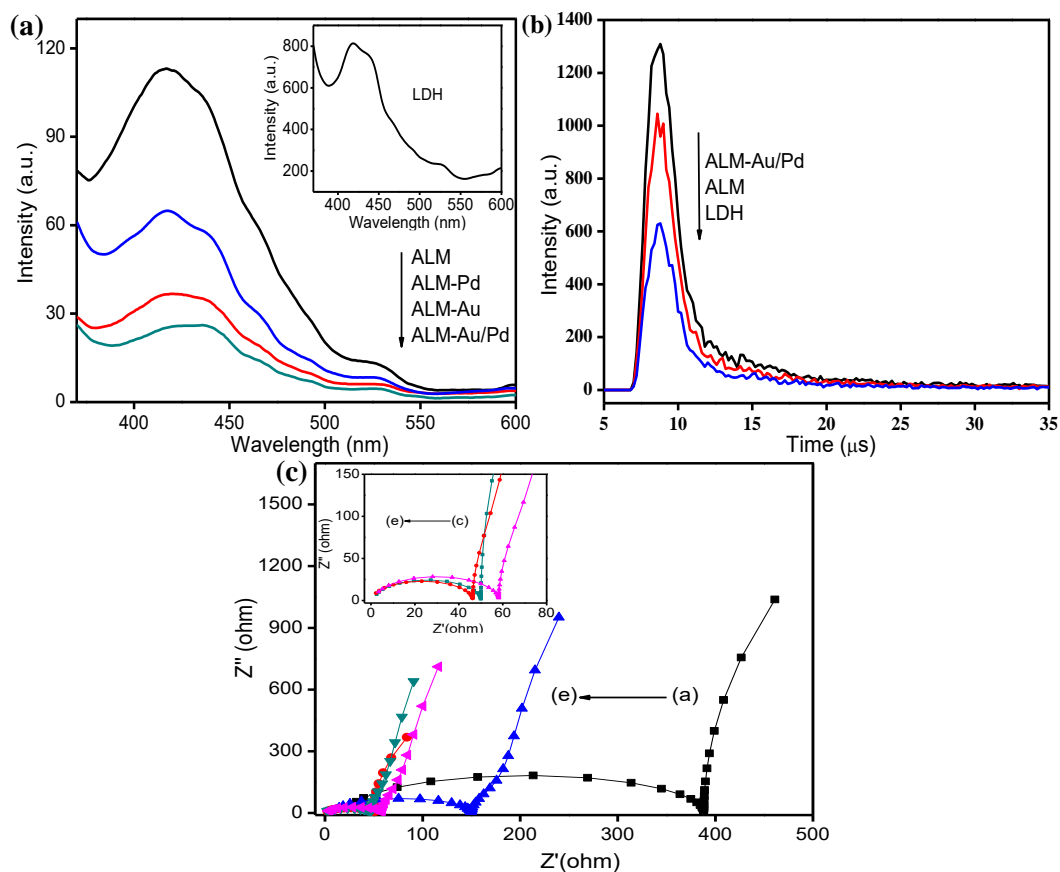


Fig. 7 (a) PL spectra of all samples (exclude MCM-41) (b) TRPL spectra of LDH, ALM and ALM-Au/Pd and (c) EIS spectra of [(a) LDH (b) ALM (c) ALM-Pd (d)ALM-Au and (e)ALM-Au/Pd].

Table 3 Photoinduced charge lifetimes of LDH, ALM and ALM-Au/Pd materials.

Catalysts	A_1 (%)	τ_1 (μ s)	A_2 (%)	τ_2 (μ s)	τ (μ s)
LDH	10.09	1.20	89.90	10.69	10.6
ALM	8.71	1.4	91.28	14.66	14.6
ALM-Au/Pd	8.46	1.51	91.53	16.32	16.20

Photoelectrochemical Study

Mott–Schottky plots were drawn to study the electronic structure, semiconducting nature and underlying mechanism of the photocatalytic reaction. As displayed in Fig. 8a, both LDH and

ALM-Au/Pd show the positive slopes in Mott–Schottky plots ($1/C^2$ versus electrode potential) which corresponds to overall shape in consistent with typical n-type semiconductors with electrons as the major charge carrier. The flat band potential (V_{fb}) can be calculated from the X-intercept obtained by extrapolating the linear portion of M-S plot by using equation (equ-7).⁶¹

$$\frac{1}{C^2} = \left(\frac{2}{q\epsilon_0\epsilon N_d} \right) \left(V_{app} - V_{FB} - \frac{kT}{q} \right) \quad (7)$$

Where, N_d the donor density, V_{app} the applied potential, ϵ the dielectric constant, ϵ_0 the permittivity of the vacuum and kT/q represents the temperature dependence term. $1/C^2 = 0$, gives the V_{FB} (flat band potential) vs Ag/AgCl electrode. The flat band potential of LDH was obtained -0.68V vs the Ag/AgCl reference electrode (-0.08V versus NHE). Generally for n-type semiconducting material, the flat band potential is situated near to its conduction band (CB) potential.⁶² Therefore the CB edge of LDH was found to be -0.08 V vs NHE and from Tauc plot, the band gap energy of LDH was found to be 2.5 eV, so the valence band (VB) potential of LDH was determined to be 2.42V vs NHE. Moreover, the smaller slope of Au/Pd-ALM compared to LDH represents a higher carrier density as well as highest donor density in the composite, which is beneficial for improved electronic conductivity within the photoanode to support efficiency of electron-hole separation. The slight negative shift in flat band potential from -0.68 V for LDH to -0.76 V in case of Au/Pd-ALM. This negative shift in flat band potential may be attributed to band unpinning with surface trapped holes, representing efficient electrode/electrolyte interface charge transfer, resulting upward shift in Fermi level by increasing the degree of band bending and deeply enhance the efficiency of photogenerated charge carriers separation and migration.⁶³

The photoelectrochemical activities of LDH, ALM, ALM-Au, ALM-Pd and ALM-Au/Pd photoelectrodes were investigated from their polarization curves by using linear sweep voltammogram (LSV) technique. As shown in Fig. 8b and 8c, all the photoelectrodes displayed anodic photocurrents owing to the n-type conductivity under visible light illumination and dark condition. It was observed that all the neat materials show comparatively small anodic current response in the applied potential window signifying poor photocatalytic behaviour compared to metal incorporated samples. However, integrating MCM-41 with LDH and upon loading of noble metal nanoparticles, the photoelectrocatalytic performance of the composite significantly increases both in dark and in presence of light.

Upon visible light irradiation all the photocatalysts possessed high photocurrent density than in dark condition. LDH, ALM, ALM-Au, ALM-Pd and ALM-Au/Pd photoelectrodes show anodic photo-current density of 2.3 mA/cm², 2.0 mA/cm², 1.4 mA/cm², 1.1 mA/cm² and 0.9 mA/cm² in the region of 0 to 1.4 V respectively with successive cathodic shift in the onset potential under the illumination of visible light. The improved photocurrent density of ALM-Au/Pd suggests that Au/Pd alloy heterostructure can efficiently accelerate the photon harvesting capability and photoconversion activity of LDH. The synergetic effect of Au/Pd alloyed nanostructure and charge heterogeneity encourage the fast separation of the photogenerated charge carrier. The faster transfer rate of photoinduced charge carriers improved electron-hole separation efficiency and increased photocurrent also. Enhanced activity is due to new active sites and Schottky barrier generated at the Au/Pd nanoparticles-semiconductor interface that facilitates the surface redox reaction.⁶⁴ Under light illumination, the excited electron could readily migrate and diffuse easily to show higher anodic current. Hence, the enhanced photoconversion activity was attributed to the synergistic effect of co-doped Au/Pd nanoalloy in increasing electron shuttling and accelerates the fast transport and separation of the photogenerated charge carrier along with less resistance offered by the photocatalyst. Moreover, the efficient of charge carriers separation in the ALM-Au/Pd also evidenced by the PL study.

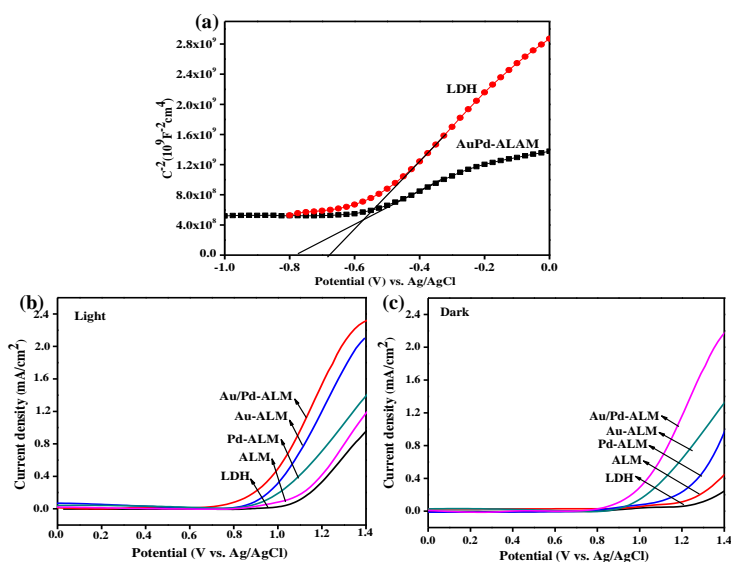


Fig. 8 MS plot of LDH and ALM-Au/Pd (a), LSV curve of all photocatalysts under light illumination (b) and dark condition (c).

Scavenger study for photocatalytic conversion

To explain the photocatalytic charge transfer mechanism, detection of active species was very important. In nitrogen atmosphere, photogenerated electrons (e^-) and holes (h^+) are the most

important reductive and oxidative reactive species for selective redox organic transformation reaction.³⁵ A control experiment was conducted over the ALM-Au/Pd nanocomposite in order to determine the effects of photoexcited h^+ and e^- on the selective synthesis of imine in the coupled photocatalytically system of benzyl alcohol oxidation and nitrobenzene reduction. In this experiment, $AgNO_3$ and TEA were used as electron and hole scavenger respectively. As shown in Fig. 9, when the TEA was introduced into the reaction system, the yield of all three products was significantly reduced from 89.6% to 40%, 20% to 8% and 68% to 16.3% for benzaldehyde, aniline and imine respectively. The decreased yield of benzaldehyde indicates h^+ is the reactive species for selective photooxidation of benzyl alcohol. In general, when the photogenerated holes are quenched in the reaction process, the recombination of charge pairs is hindered and the corresponding photoinduced electrons are available for the reduction reaction. But in the present system, the lower yield of aniline in compared to control experiment suggests the reduction of nitrobenzene depends on the oxidation of benzyl alcohol. This may be due to those protons (H^+) generated during the photooxidation of benzyl alcohol, responsible for the reduction of nitrobenzene into aniline. Moreover lower yield of benzaldehyde and aniline could not able to produce more amount of imine. However, with the addition of $AgNO_3$ as e^- scavenger, the yields of imine (29.8%) and aniline (9.9%) were remarkably decreased but the benzaldehyde quantity slightly enhanced from 89% to 90.4%. From the above quenching experiments, it was concluded that the photoinduced h^+ and e^- are decisive factors in the imine synthesis through photocatalytic conversion of benzyl alcohol and nitrobenzene respectively.

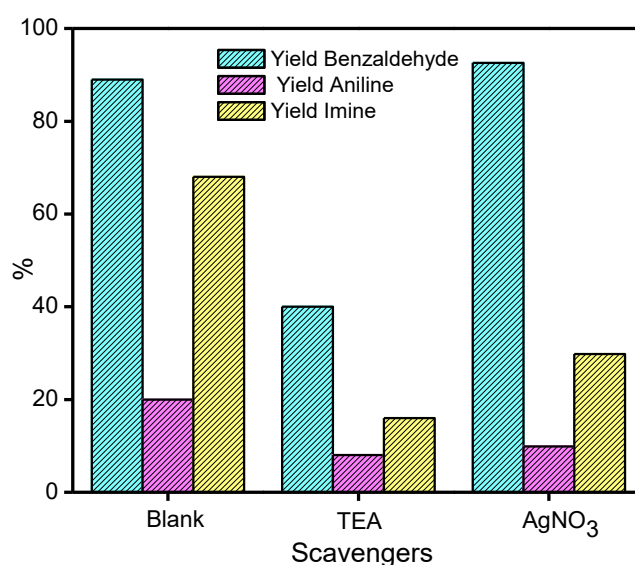
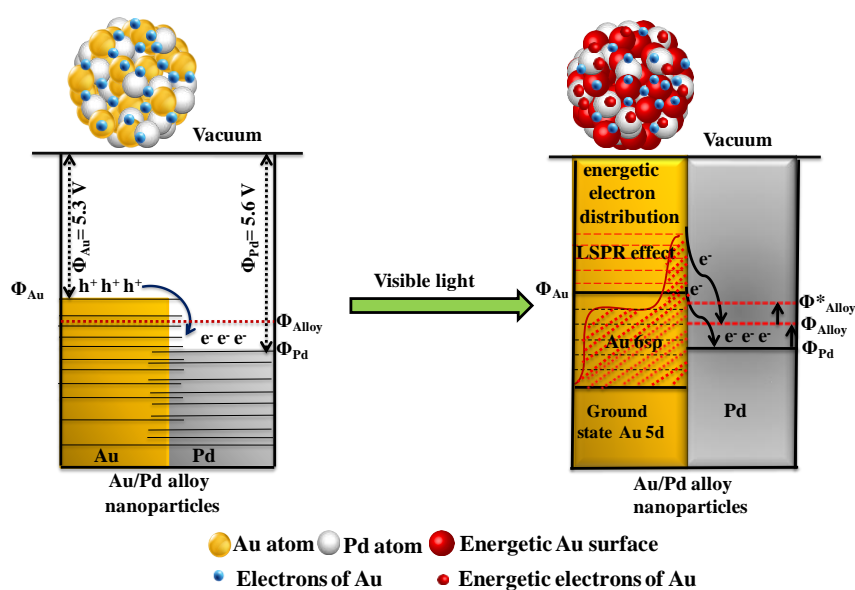


Fig. 9 Benzyl alcohol and nitrobenzene conversion rate over ALM-Au/Pd in the presence of various radical scavengers

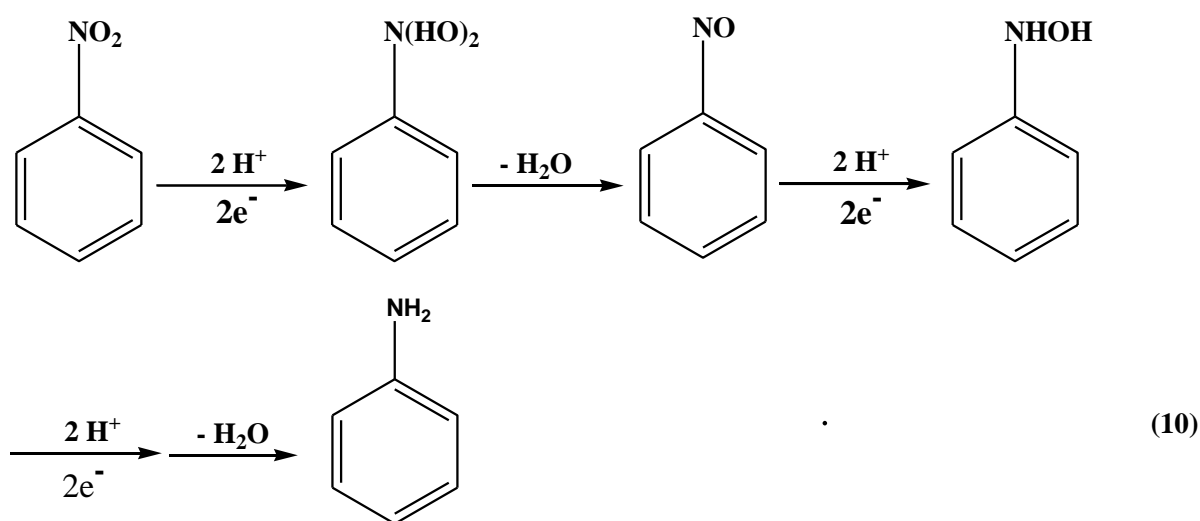
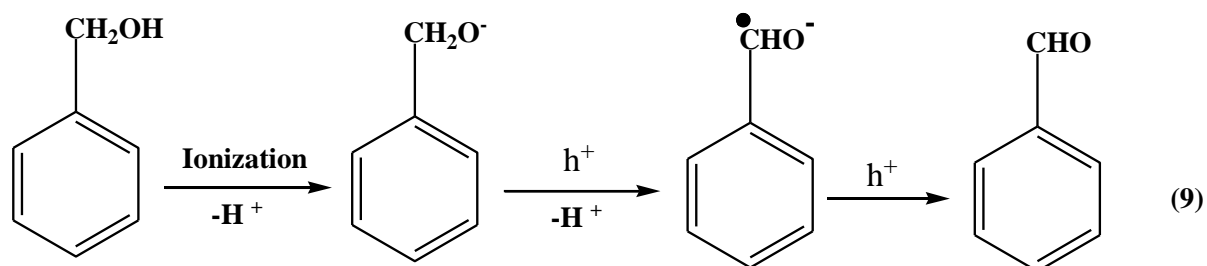
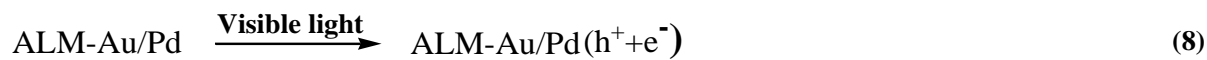
Imine synthesis through photocatalytic charge transfer Mechanism

Based on the above results and discussion, A possible mechanism for imine formation via tandem photocatalytic conversion of benzyl alcohol and nitrobenzene followed by coupling between benzaldehyde and aniline over ALM-Au/Pd photocatalyst was proposed (scheme 3). The proposed photocatalytic mechanism explains the synergistic effect between the Au/Pd alloy nanostructure and LDH in ALM-Au/Pd nanocomposite. The imine synthesis was first achieved by oxidation of benzyl alcohol followed by reduction of nitrobenzene. When the ALM-Au/Pd is irradiated and excited by the visible photons the electron of the VB are excited into the CB of LDH and then rapidly transferred to Au/Pd alloy sites as the Au/Pd bimetallic alloy having higher electron-capturing tendency due to its low-lying of Fermi level.¹⁴ This electron migration could result in the creation of a metal-semiconductor Schottky junction which can efficiently trap the photogenerated electrons and assist the electron-hole separation, thus accelerates the photocatalytic activity. In addition, upon visible light irradiation, the photons were absorbed by Au/Pd alloyed nanoparticle through LSPR excitation, resulting hot electrons on alloy surface. Subsequently, the hot electrons of Au and photogenerated electrons of LDH together transferred to the Pd site. As depicted in Scheme 2, the work function ($\Phi_{\text{Pd}} = 5.6$) of Pd is a little larger than the work function of Au ($\Phi_{\text{Au}} = 5.3$). Under visible light illumination, in alloyed nanostructure when the two metals are in contact with each other, in order to achieve equilibrium (Φ^*_{alloy}) the energetic electrons will flow from Au to Pd for establish an equal chemical potential gradient. Owing to this charge redistribution Pd atom becomes rich in electron and Au atom electronically deficient. This heterogeneity in charge distribution enhanced the interaction between reactant molecules (benzyl alcohol and nitrobenzene) and Au/Pd alloy nanoparticle, independent of electrophilic/nucleophilic nature of the reactants. The close interaction leads to decrease in activation energy and ultimately increase the rate of photocatalytic reaction. In the same time, the positively charged photogenerated holes could accumulate in the VB of LDH. The Bronsted and Lewis surface basic sites of ALM-Au/Pd helps to facilitate the deprotonation of surface adsorbed benzyl alcohol and to form alkoxide anions. Then alkoxide anions reacts with the photogenerated holes at VB of LDH to form carbon radicals by releasing another H^+ . The obtained carbon radical further react with photogenerated hole to form benzaldehyde. Subsequently, electrons gather at Au/Pd bimetallic alloy nanoparticle and presence of H^+ generated during oxidation process could efficiently reacts with nitrobenzene to form nitrosobenzene and H_2O molecule. After that, the nitrosobenzene gradually convert into the aniline as the reaction progresses. Finally, benzaldehyde couple with aniline to produce imine

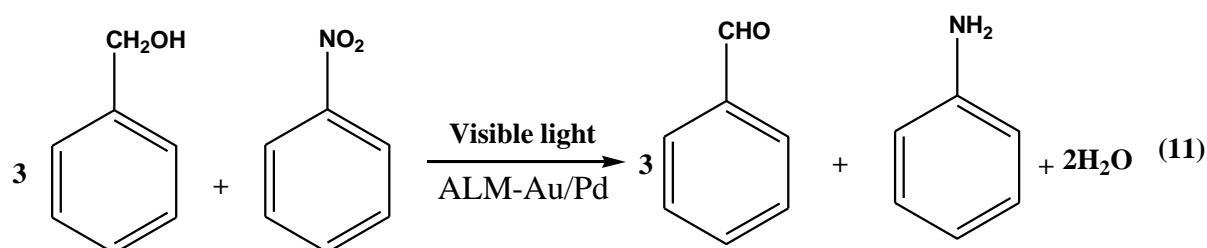
by discharging water. Mainly the released hydrogen during the conversion of benzyl alcohol to benzaldehyde are hydroxyl hydrogen and α -hydrogen of benzyl alcohol, respectively, and the imine hydrogen is initiated from benzaldehyde. This organic transformation reaction indicates the photocatalytic oxidation of benzyl alcohol to benzaldehyde involves 2 photogenerated holes and the photocatalytic reduction of nitrobenzene to aniline requires 6 electrons and 6 proton (H^+). This 6 mol of protons are generated from 3 mol of benzyl alcohol. Therefore, according to theoretical calculation, the amount of benzyl alcohol should be three times of nitrobenzene. Moreover 1 mol imine is produced by condensation reaction between 1 mol benzaldehyde and 1 mol aniline.^{35,65} So after the completion of tandem reaction, the concentration of produced benzaldehyde should be two times of imine. The detailed photocatalytic organic reaction mechanism was explained by following equations (equ-8-12). Thus it is make clear that the formation of imine is definitely synthesized from benzyl alcohol and nitrobenzene in the current photocatalytic reaction system.

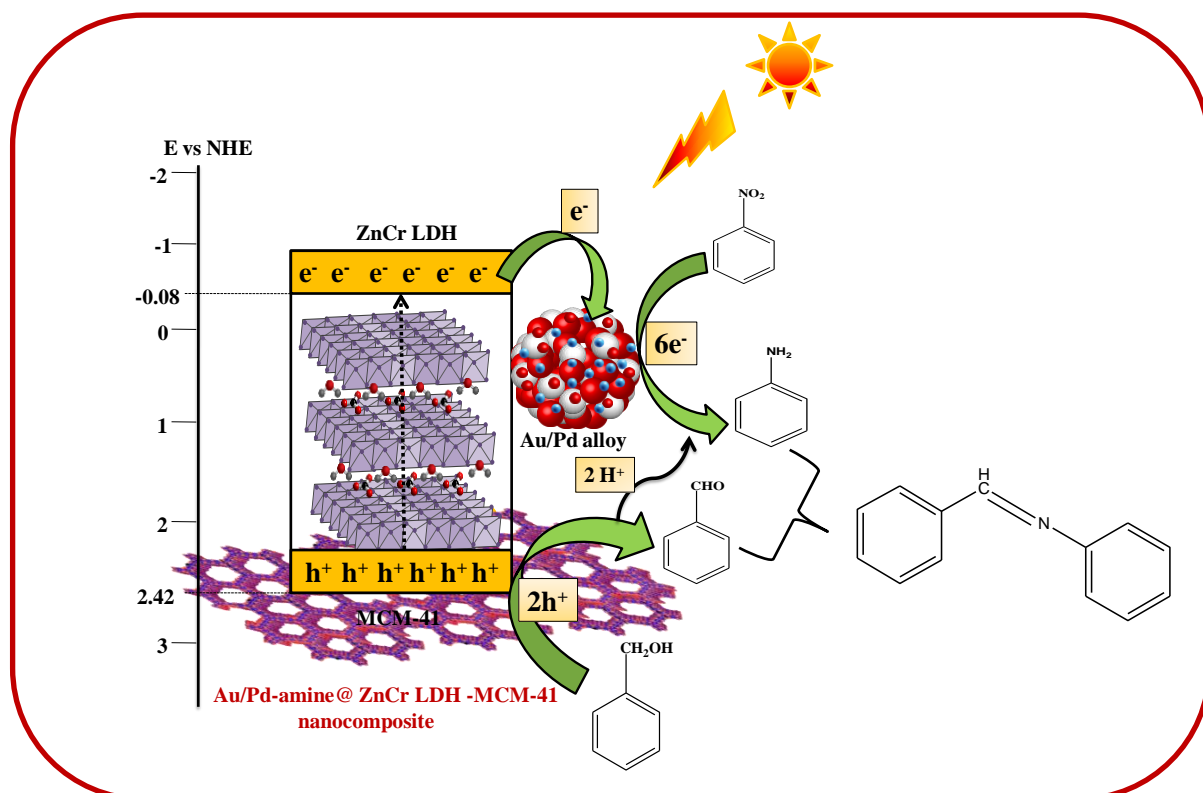
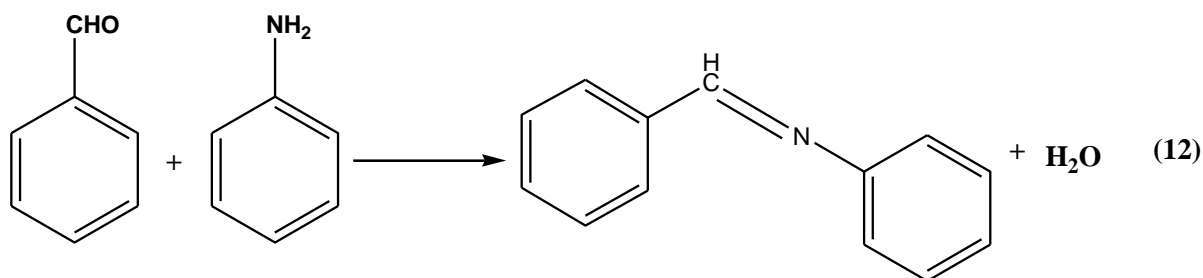


Scheme 2. The impact of alloying with visible light illumination of Au/Pd alloy nanoparticles. [The surface electronic behaviour of the Au/Pd alloy nanoparticle are unlike from single Au and Pd nanoparticle. The Pd sites having more electron density than Au site because Pd has a slightly greater work function ($\Phi_{Pd} = 5.6$) than the Au ($\Phi_{Au} = 5.3$). To maintaining the Fermi level equilibrium, the electrons will move from Au to Pd site and consequently the electronic chemical gradient between two metals are equal (Φ_{alloy}). After the light absorption by Au nanoparticle in Au/Pd alloy the resulting energetic electron (hot electrons) are transfer from Au to Pd. The Fermi level of alloy nanoparticle without light illumination is lower than under light illumination (Φ^*_{alloy})].



Over all reaction:





Scheme 3. Photocatalytic one-pot imine synthesis mechanism from Benzyl alcohol and nitrobenzene over ALM-Au/Pd nanocomposite.

Stability and reusability of photocatalyst

The stability of photocatalyst in photocatalysis reaction is an important parameter. Therefore to evaluate the stability and reusability of ALM-Au/Pd photocatalyst for synthesis of imines through photoalkylation of benzyl alcohol with nitrobenzene, the reusability experiments over ALM-Au/Pd photocatalyst was studied under visible light irradiation for 12h. After each run, the colloidal suspension was washed with distilled water and ethanol for next run. The results was summarised in Fig. 10a. It indicates that yield of benzyldehyde, imine and aniline do not show distinct change during the first two cycles, and then it shows slight decreasing trend in next two cycles. This may be due to partial loss of the catalysts during isolation. To

investigate the photo stability of the sample, the fresh and the used photocatalysts were studied by XRD and TEM analysis. As shown in Fig. 10b it was clearly seen after the light illumination, the intensity of used ALM-Au/Pd nanocomposite slightly reduced than fresh catalyst otherwise there was no structurally changed between them. Similarly the TEM images (Fig.10c) of reused ALM-Au/Pd sample shows an unchanged morphology even after 4th run. The Au/Pd alloys were not leach out from the ALM surface after the visible light irradiation. Further, the photoelectrochemical stability and resistance of the catalyst was investigated by CA study. Fig. 10d displayed the corresponding chronoamperometric response of time dependence anodic photocurrent of LDH, ALM, ALM-Pd, ALM-Au, and ALM-Au/Pd. When all the photocatalyst was irradiated with light, the anodic photocurrent was found to decrease slowly in ALM-Au/Pd nanocomposite than other photocatalyst and then became relatively stable with time even after 300s. The results of current density exhibit a very slow attenuation and indicate that photocorrosion or reduction of the photoanodes might not occur during the reaction. From the above results it can be concluded that ALM-Au/Pd nanocomposite is a highly stable and reusable visible light-driven photocatalyst for one-pot imine synthesis through benzaldehyde and aniline.

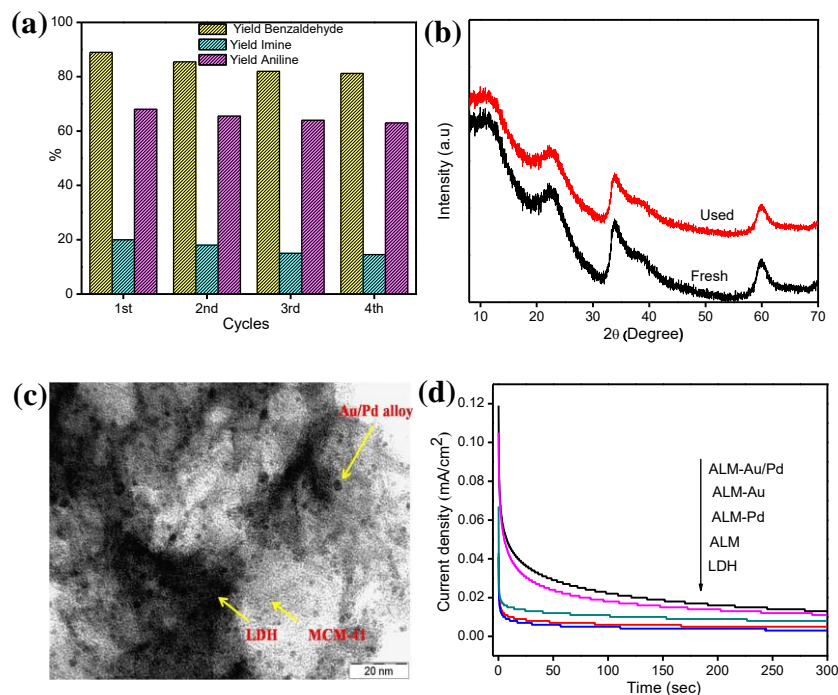


Fig. 10 Reusability study of (a) imine synthesis in four consecutive cycles of run in every 3 h for ALM-Au/Pd nanocomposite, (b) XRD plot ALM-Au/Pd after and before the photocatalytic reaction, (c) TEM image of ALM-Au/Pd after light irradiation and (d) CA curve of all photocatalysts.

Conclusion

Herein, we have successfully synthesised ALM-Au/Pd catalyst and exploited the photocatalytic activity towards one-pot conversion of benzyl alcohol and nitrobenzene to imine under visible-light irradiation. Introduction of MCM-41 into the LDH with functionalisation of amine group provides high surface area and Bronsted basic sites for photocatalytic reaction. The amine groups helps in controlling the dispersion and size of Au/Pd alloy nanoparticles on the LM surface, the metal–ligand support interaction, serves active sites for the photocatalytic organic transformation reaction. That surface heterogeneity by loading alloyed Au/Pd nanoparticles strongly interacts with reactant molecules and can remarkably improve the reaction activity. In situ formation of imines under visible light irradiation proceeds via a redox reaction pathway involving sequentially benzyl alcohol oxidation and nitrobenzene reduction. This work represents the concept of integrating the newly design bimetal alloyed nanoheterostructure for tandem photoconversion reaction resulted to imine synthesis which may be an eco-friendly and competent organic synthesis process as an alternative of traditional industrial synthesis procedure.

Acknowledgements

The authors are very much thankful to the management of SOA University for their encouragement and support. Mr. Sriram Mansingh and Mr. Kundan Kumar Das (CNSNT, ITER, SOA Deemed to be University) are greatly acknowledged for their technical support

References

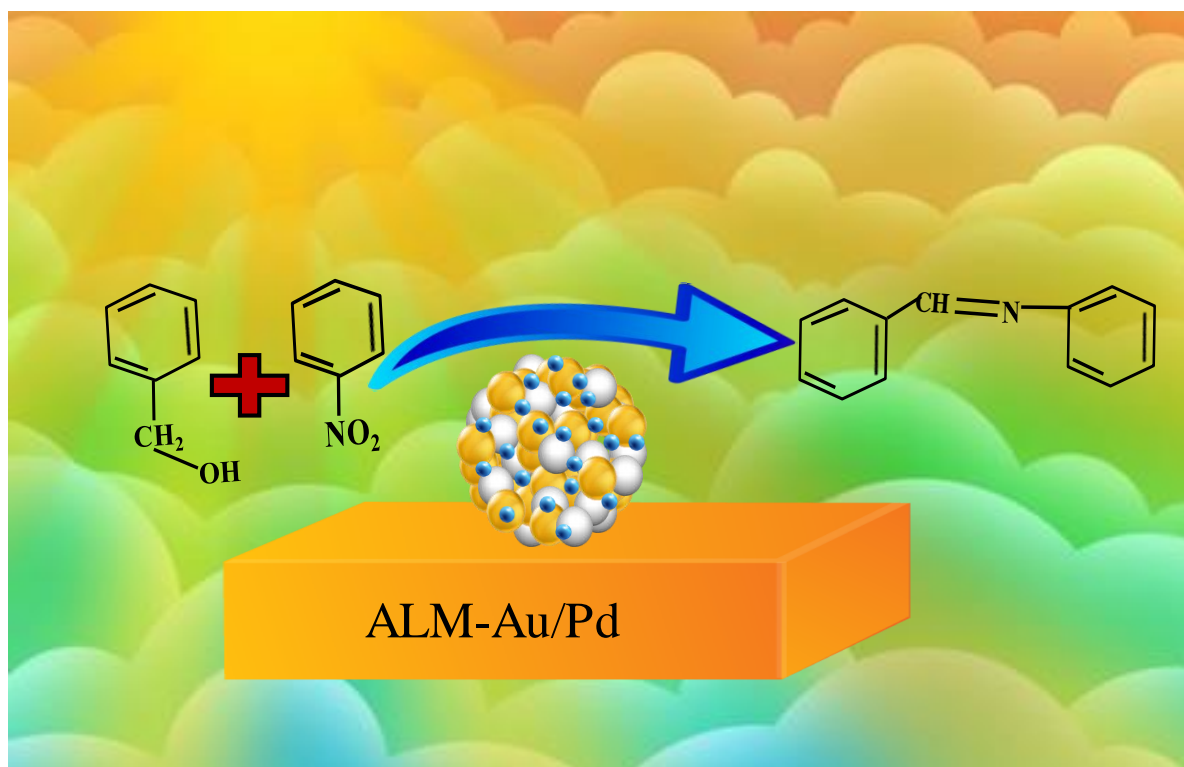
1. D. Patil and S. Adimurthy, *Asian J. Org. Chem.*, 2013, **2**, 726–744.
2. X. Lang, X. Chena and J. Zhao, *Chem. Soc. Rev.*, 2014, **43**, 473-486.
3. C. A. Newman, J. C. Antilla, P. Chen, A. V. Predeus, L. Fielding and W. D. Wulff, *J. Am. Chem. Soc.*, 2007, **129**, 7216–7217.
4. J. S. M. Samec, A. H. Ell and J.-E. Backvall, *Chem. Eur. J.*, 2005, **11**, 2327–2334.
5. J. -R. Wang, Y. Fu, B. -B. Zhang, X. Cui, L. Liu and Q. -X. Guo, *Tetrahedron Lett.*, 2006, **47**, 8293–8297.
6. H. Yuan, W. -J. Yoo, H. Miyamura and S. Kobayashi, *J. Am. Chem. Soc.*, 2012, **134**, 13970–13973.

7. H. Hirakawa, M. Katayama, Y. Shiraishi, H. Sakamoto, K. Wang, B. Ohtani, S. Ichikawa, S. Tanaka and T. Hira, *ACS Appl. Mater. Interfaces*, 2015, **7**, 3797–3806.
8. Y. Shiraishi, K. Fujiwara, Y. Sugano, S. Ichikawa and T. Hirai, *ACS Catal.*, 2013, **3**, 312–320.
9. C. Gunanathan, Y. Ben-David and D. Milstein, *Science*, 2007, **317**, 790–792.
10. A. A. Melvin, K. Illath, T. Das, T. Raja, S. Bhattacharyya, and C. S. Gopinath, *Nanoscale*, 2015, **7**, 13477–13488.
11. P. Devaraji, N. K. Sathu, and C. S. Gopinath, *ACS Catal.*, 2014, **4**, 2844–2853.
12. Q. Xiao, S. Sarina, E. Jaatinen, J. Jia, D. P. Arnold, H. Liuc and H. Zhu, *Green Chem.*, 2014, **16**, 4272–4285.
13. T. Jiang, C. Jia, L. Zhang, S. He, Y. Sang, H. Li, Y. Li, X. Xu and H. Liu, *Nanoscale*, 2015, **7**, 209–217.
14. Y. Zhang and S. –J. Park, *J. Catal.*, 2017, **355**, 1–10.
15. P. Fageria, S. Uppala, R. Nazir, S. Gangopadhyay, C.-H. Chang, M. Basu and S. Pande, *Langmuir*, 2016, **32**, 10054–10064.
16. M. Wen, K. Mori, Y. Kuwahara, and H. Yamashita, *ACS Energy Lett.*, 2017, **2**, 1–7.
17. W. Y. Hernández, J. Lauwaert, P. V. D. Voort and A. Verberckmoes, *Green Chem.*, 2017, **19**, 5269–5302.
18. M.J. Climent, A. Corma, S. Iborra and A. Velty, *J. Catal.*, 2004, **221**, 474–482.
19. A. Takagaki, M. Takahashi, S. Nishimura and K. Ebitani, *ACS Catal.*, 2011, **1**, 1562–1565.
20. E. Li, Z. Xu and V. Rudolph, *Appl. Catal. B*, **2009**, **88**, 42–49.
21. L. Mohapatra and K.M. Parida, *J. Mater. Chem. A*, 2016, **4**, 10744–10766.
22. Z. Wang, Y. Song, J. Zou, L. Li, Y. Yu and L. Wu, *Catal. Sci. Technol.*, 2018, **8**, 268–275.
23. L. Sobhana, M. Sarakha, V. Prevot and P. Fardima, *Appl. Clay Sci.*, 2016, **134**, 120–127.
24. Z. Gao, R. Xie, G. Fan, L. Yang and F. Li, *ACS Sustainable Chem. Eng.*, 2017, **5**, 5852–5861.
25. M. Sahoo and K.M. Parida, *Appl. Catal. A*, 2013, **460–461**, 36–45.
26. S. Singha, M. Sahoo and K. M. Parida, *Dalton Trans.*, 2011, **40**, 7130–7132.
27. D. P. Sahoo, D. Rath, B. Nanda and K. M. Parida. *RSC Adv.*, 2015, **5**, 83707–83724.

28. P. Trens, M. L. Russell, L. Spjuth, M. J. Hudson and J. –O. Liljenzin, *Ind. Eng. Chem. Res.*, 2002, **41**, 5220–5225.
29. K.M. Parida and D. Rath. *J. Mol. Catal.*, 2009, **310**, 93–100.
30. X. Jin, K. Taniguchi, K. Yamaguchi and N. Mizuno, *Chem. Sci.*, 2016, **7**, 5371-5383.
31. A.-Y. Park, H. Kwon, A. J. Woo and S.-J. Kim, *Adv. Mater.*, 2005, **17**, 106-109.
32. L. Kuai, X. Yu, S. Wang, Y. Sang, and B. Geng, *Langmuir*, 2012, **28**, 7168–7173.
33. F. Gao and D. W. Goodman, *Chem. Soc. Rev.*, 2012, **41**, 8009-8020.
34. R. Ferrando, J. Jellinek, and R. L. Johnston, *Chem. Rev.*, 2008, **108**, 845–910.
35. Y. Wua, X. Ye, S. Zhang , S. Meng, X. Fu and X. Wang, X. Zhang and S. Chen, *J. Catal.*, 2018, **359**, 151-160.
36. N. Baliarsingh, L. Mohapatra and K.M. Parida, *J. Mater. Chem. A*, 2013, **1**, 4236-4243.
37. D. P. Sahoo, S. Patnaik, D. Rath, B. Nanda and K. M. Parida, *RSC Adv.*, 2016, **6**, 112602- 112613.
38. C. Li, H. Lu, Y. Lin, X. Xie, H. Wanga and Linjiang Wang, *RSC Adv.*, 2016,**6**, 97237-97240.
39. X. Wang, Q. Liu, Z. Xiao, X. Chen, C. Shi, S. Tao, Y. Huang and C. Liang, *RSC Adv.*, 2014,**4**, 48254-48259.
40. Y. W. Lee, N. H. Kim, K. Y. Lee, K. Kwon, M. Kim and S. W. Han, *J. Phys. Chem. C.*, 2008, **112**, 6717-6722.
41. J. F. Sanchez-Ramirez, *Superficies y Vacio*, 2001, **13**, 114-116.
42. P. A. Bharad, K. Sivaranjani, and C. S. Gopinath, *Nanoscale*, 2015,**7**, 11206-11215 .
43. K. Sivaranjani and C. S. Gopinath, *J. Mater. Chem.*, 2011, **21**, 2639-2647.
44. D. B. Nale, D. Rath, K. M. Parida, A. Gajengia and B. M. Bhanagea, *Catal. Sci. Technol.*, 2016, **6**, 4872-4881.
45. K. M. Parida and L. Mohapatra, *Chem. Eng. J.*, 2012, **179**, 131–139.
46. N. Dimitratos, A. Villa, D. Wang, F. Porta, D.S. Su and L. Prati, *J. Catal.*, 2006, **244**, 113–121.
47. D. Wang, A. Villa, F. Porta, D.S. Su and L. Prati, *Chem. Commun.*, 2006, **0**, 1956-1958.
48. A. C. Pradhan, Binita Nanda and K. M. Parida, *Dalton Trans.*, 2011, **40**, 7348- 7356.
49. D. B. Nale, S. Ranab, K.M. Parida and B. M. Bhanagea, *Appl. Catal. A*, 2014, **469** 340– 349.
50. K.M, Parida and L. Mohapatra, *Dalton Trans.*, 2012, **41**, 1173-1178.

51. B. Lu and K. Kawamoto, *Catal. Sci. Technol.*, 2014, **4**, 4313-4321.
52. K. M. Cho, K. H. Kim, K. Park, C. Kim, S. Kim, A. Al-Saggaf, I. Gereige and H. -T. Jung, *ACS Catal.*, 2017, **7**, 7064–7069.
53. Y. Zhang, X. He, J. Ouyang and H. Yang, *Sci Rep.*, 2013, **3**, 2948.
54. J. Ederer, P. Janos, P. Ecorchard, J. Tolasz, V. Stengl, H. Benes, M. Perchacz and O. Pop-Georgievski, *RSC Adv.*, 2017, **7**, 12464- 12473.
55. C. Wang, B. Ma, S. Xu, D. Li, S. He, Y. Zhao, J. Han, M. Wei, D. G. Evans and X. Duan, *Nano Eng.*, 2017, **32**, 463-469.
56. M. Lan, G. Fan, L. Yang and F. Li, *Ind. Eng. Chem. Res.*, 2014, **53**, 12943–12952.
57. Y. Nakaia, M. Azumaa, M. Muraokaa, H. Kobayashib and S. Higashimoto, *Mol. Catal.*, 2017, **443**, 203–208.
58. Y. Shiraishi, M. Ikeda, D. Tsukamoto, S. Tanaka and T. Hirai, *Chem. Commun.*, 2011, **47**, 4811-4813.
59. Y. Shiraishi, M. Ikeda, D. Tsukamoto, S. Tanaka and T. Hirai, *Chem. Commun.*, 2011, **47**, 4811-4813.
60. S. Nayak, L. Mohapatra and K. M. Parida, *J. Mater. Chem. A*, 2015,**3**, 18622-18635.
61. M. Gratzel, *Nature*, 2001, **414**, 338 –344.
62. L. Ye, D. Wang and S. Chen, *ACS Appl. Mater. Interfaces*, 2016, **8**, 5280–5289.
63. N. Bhandary, A. P. Singh, S. Kumar, P. P. Ingole, G. S. Thakur, A. K. Ganguli and S. Basu, *ChemSusChem*, 2016, **9**, 2816-2823.
64. A. Furube, L. Du, K. Hara, R. Katoh and M. Tachiya, *J. Am. Chem. Soc.*, 2007, **129**, 14852–14853.
65. C. Ling, X. Ye, J. Zhang, J. Zhang, S. Zhang, S. Meng, X. Fu and S. Chen, *Sci Rep.*, 2017, **7**, 27.

TOC image



Au/Pd loaded amine functionalised ZnCr LDH-MCM-41 nanocomposite for visible light induced organic transformation towards one-pot imine synthesis.

Supporting information

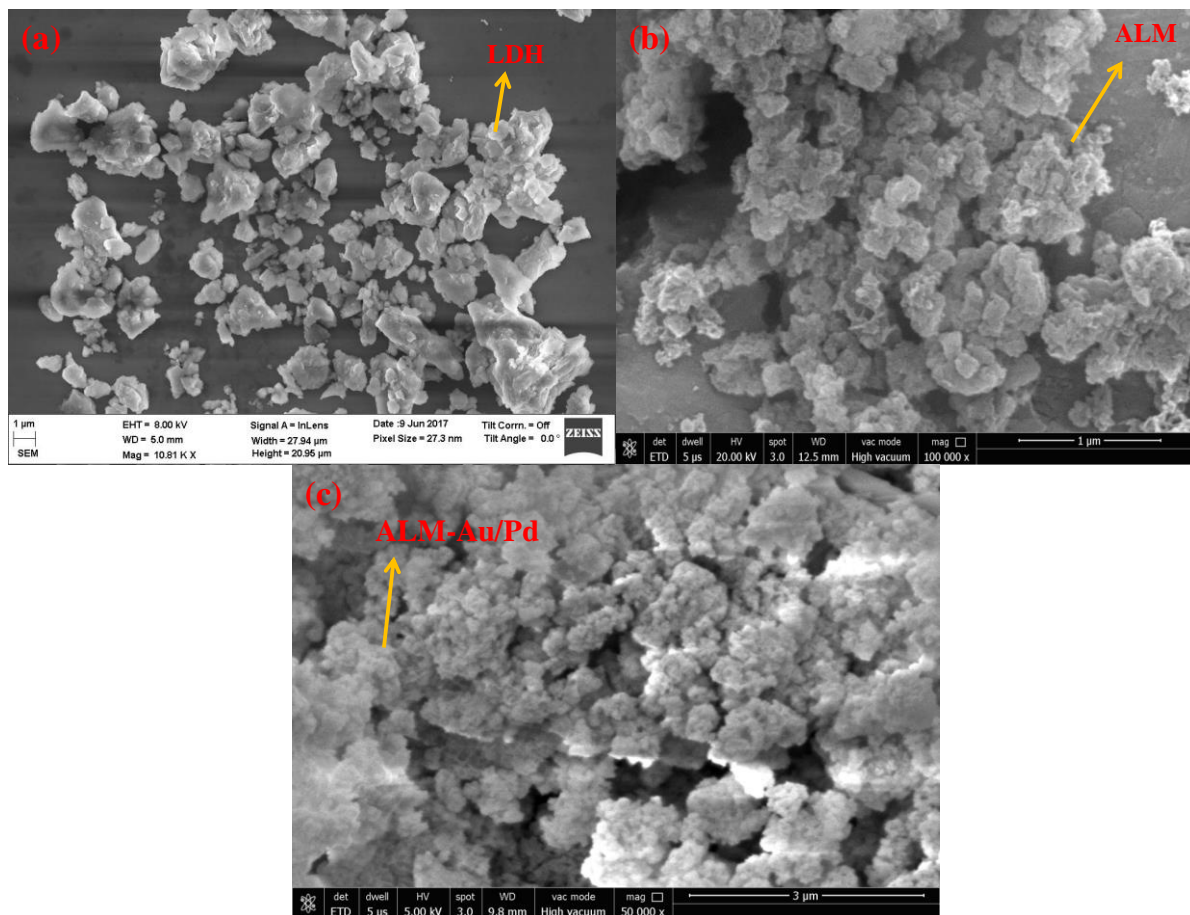
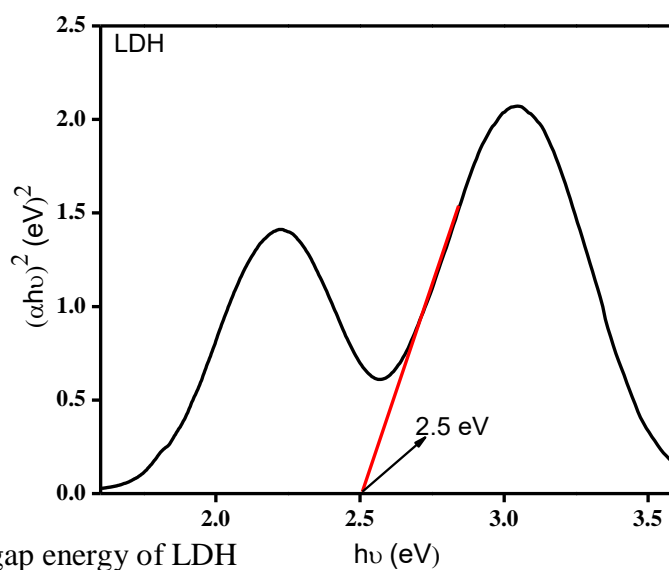
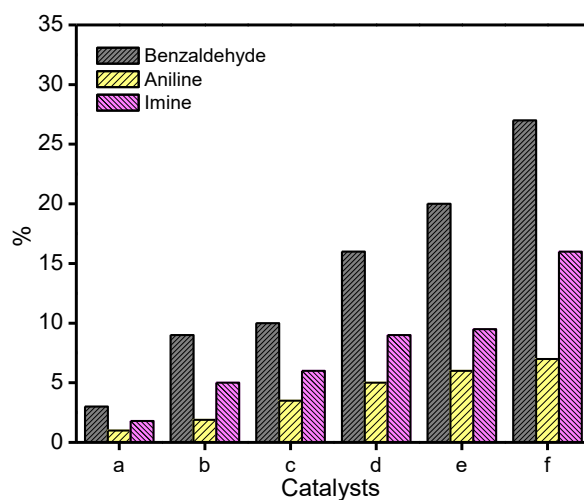
Influence of Au/Pd alloy on amine functionalised ZnCr LDH-MCM-41 nanocomposite; a visible light sensitive photocatalyst for one-pot Imines synthesis**Fig. S1** SEM images of (a)LDH, (b)ALM and (c)ALM-Au/Pd**Fig. S2** Band gap energy of LDH

Table. S1 photocatalytic benzyl alcohol conversion

Catalysts	Benzyl alcohol Conversion (%)	Benzaldehyde Yield(%)	Benzaldehyde Selectivity(%)
AL _{0.2} M	19	17	79
AL _{0.33} M	27	24.5	85
AL _{0.5} M	35.5	33.7	88
ALM	48.7	46	88

Table. S2 photocatalytic one-pot imine synthesis from benzyl alcohol and nitrobenzene conversion

Catalysts	Conversion (%)		Yield (%)		
	Benzyl alcohol	Nitrobenzene	Benzaldehyde	Aniline	Imine
MCM-41	11	12.8	5.1	2	3.9
LDH	48	53.1	45	15	22
ALM	56.3	62	51.3	22	31
ALM-Pd	71	75	68	23	47.6
ALM-Au	82.8	86.4	77	23.7	51.3
ALM-Au/Pd	96	99	89	20	68

**Fig. S3** Yield of benzaldehyde, aniline and imine over (a) MCM-41, (b) LDH, (c) ALM, (d)ALM-Pd, (e) ALM-Au and (f) ALM-Au/Pd under dark condition.